Dynamic Proximal Interactomics and Chemical Genetic Screening Reveal CCR4-NOT Sequestration in Stress Granules as a Mechanism for Transcript Stabilization

Yi-Cheng Tsai[1,2,3], Hiroyuki Uechi[4,7], Sean R. Millar[1,2], Eileigh Kadijk[1], Karl J. Schreiber[1], Alon Minkovich[1,2], Jie Qi Huang[1,2], Zhixin Zhang[5], Rico Barsacchi[6,7], Claudia Möbius[6,7], Antje Janosch[6,7], Jonathan C. Savage[7], Hannes Röst[2,3], Anthony A. Hyman[7,8*], Ji-Young Youn[1,2,8,9*]

[1] Program in Molecular Medicine, The Hospital for Sick Children, Toronto, ON M5G 0A4, Canada.

[2] Department of Molecular Genetics, University of Toronto, Toronto, ON M5S 1A8, Canada.

[3] Terrence Donnelly Centre for Cellular Biomolecular Research, University of Toronto, Toronto, ON M5S 3E1, Canada.

[4] Frontier Research Institute for Interdisciplinary Sciences, Tohoku University, Sendai, Japan

[5] 4+4 Medical Doctor Program, Chinese Academy of Medical Sciences and Peking Union Medical College, Beijing, China.

[6] Max Planck Institute of Molecular Cell Biology and Genetics, Technology Development Studio, 01307, Dresden, Germany.

[7] Max Planck Institute of Molecular Cell Biology and Genetics, 01307, Dresden, Germany

[8] Senior Author

[9] Lead Contact: jiyoung.youn@sickkids.ca

* Corresponding authors

KEYWORDS: stress granules, CCR4-NOT complex, poly(A) tail regulation, condensate proteome, protein localization, proximity-dependent biotinylation, lipoamide, data-independent acquisition.

Data deposition: Mass spectrometry data have been deposited in the Mass spectrometry Interactive Virtual Environment (MassIVE, http://massive.ucsd.edu).

MassIVE ID: MSV00009595 (ftp://massive.ucsd.edu/v08/MSV000095953/)

MassIVE ID: MSV000095944 (ftp://massive.ucsd.edu/v08/MSV000095944/)

ABSTRACT

Living cells adapt to stress by protecting essential resources, such as stabilizing transcripts. Stress granules, which form during stress through the coalescence of polyadenylated transcripts released from polysomes and RNA-binding proteins, are implicated in post-transcriptional regulation, although their precise roles remain contested. To address this, we generated dynamic proteomic landscapes of stress granules during assembly and disassembly under oxidative and hyperosmotic stress using multi-bait BioID profiling combined with quantitative mass spectrometry. Our analysis reveals dynamic rewiring of stress granule proximal interaction networks, identifying RNA-binding proteins involved in translation repression and mRNA decay, including the CCR4-NOT deadenylase complex, as universal molecular signatures of condensed stress granules. Using the CCR4-NOT deadenylase complex as a model, we demonstrate the function of dynamic components associated with stress granules. Complementary genome-wide chemical genetic screening identified CCR4-NOT components as regulators of stress granule formation. Reduced CCR4-NOT activity, which lengthens poly(A) tails, enhanced stress granule assembly, while shortened poly(A) tails inhibited it. Furthermore, stress-induced sequestration of the CCR4-NOT complex to stress granules coincided with known global poly(A) tail lengthening. These findings suggest that stress granule condensation promotes transcriptome stabilization by regulating CCR4-NOT localization as part of an adaptive stress response. This work underscores the power of integrating quantitative proteomics with chemical genetics to advance our understanding of biomolecular condensates in diverse biological processes.

49 **MAIN**

50 Living organisms have evolved mechanisms to survive unfavourable conditions. At the cellular level,
51 adaptation to stress involves rewiring transcriptional programming, translation control, signaling,
52 metabolism, and the reorganization of subcellular proteomes. Cells shift biological processes to conserve
53 resources during stress, slowing global transcription and translation to minimize energy consumption while
54 actively transcribing genes involved in stress responses[1,2].

55 Cellular adaptation involves changes in the subcellular proteome organization[3-5]. Advances in spatial
56 proteomics, including imaging-based microscopy and mass spectrometry, have enabled the identification
57 of proteins localized to specific subcellular compartments[4,6-12]. During stress, proteins dynamically
58 exchange between compartments[5,13-16]; however, assigning functional roles to these localization changes
59 remains challenging.

60 The re-organization of subcellular proteomes often involves the formation of membraneless organelles
61 or biomolecular condensates, which concentrate biomolecules through liquid-liquid phase separation[17-20].
62 By enriching specific biomolecules, biomolecular condensates can increase or decrease biochemical
63 reactions, buffer protein concentrations, sense environmental changes, and provide mechanical forces[21-
64 25]. Stress granules are cytosolic biomolecular condensates or RNA granules that transiently form in
65 response to various stress conditions, often as a product of global translation shutdown and release of
66 mRNAs from the polysome pool[26,27]. Stress granules host hundreds of proteins and several thousands of
67 transcripts[28-31] and are central to stress response, linking translation control to signaling and immune
68 responses[29,32,33]. They host antiviral responses during viral infection[27] and sequester regulators of cell
69 death[34,35] or cell growth pathway components during stress[36]. However, their precise role in post-
70 transcriptional regulation remains unclear.

71 A key aspect of the stress response is preserving nascent transcripts[37-40], making them ready for
72 deployment after stress cessation[41]. Among known mechanisms contributing to transcript stabilization are
73 the relief of microRNA-mediated regulation[42] and the formation of G-quadruplex structures in the 3' UTR[40].
74 While these are specific examples of stabilization, they do not explain the global stabilization of the mRNA
75 pool.

76 A key mechanism for transcript stabilization is thought to involve extending poly(A) tails, which are
77 crucial for protecting mRNA from decay[43]. Acute stress induces global poly(A) tail lengthening[44-47],
78 governed by a balance between the action of cytoplasmic polyA binding element (CPEB) proteins that
79 elongate these tails and deadenylases (such as the CCR4-NOT and PAN2-3 complexes) that shorten
80 them[43,48]. While stress-induced stabilization of transcripts has been linked to inhibiting deadenylation[38,46],
81 the molecular mechanisms behind poly(A) tail lengthening and transcriptome stabilization remain elusive.
82 Recent work has demonstrated that poly(A) tail extension is a prerequisite for stress granule formation[49],
83 hinting at a potential link between stress response and the regulation of enzymes controlling poly(A)
84 lengths. However, clear evidence connecting poly(A) tail regulatory pathways to stress responses remains
85 limited.

86 Recently, multi-bait proteomics has become a powerful approach for studying protein localization within
87 condensates[50,51]. In this study, we use multi-bait BioID time course experiments to map the proximal
88 interactome of stress granule proteins, providing a resource that captures proteomic landscape changes
89 during stress. Leveraging this resource, we demonstrate that interactions with the CCR4-NOT complex shift
90 dynamically in response to stress. Complementary genome-wide CRISPR screens against stress granule-
91 inhibiting chemical lipoamide revealed that the removal of CCR4-NOT stabilizes stress granules through
92 poly(A) tail lengthening. Microscopy analysis of CCR4-NOT showed poor localization to P-bodies, contrary
93 to its annotation, but strong localization to stress granules during stress. We propose that stress granules
94 sequester the CCR4-NOT complex, suppressing its activity and facilitating global poly(A) tail lengthening
95 and transcript stabilization as an adaptive response.

96

97 **RESULTS**

98 **Dynamic Changes in Proximal Interactions of Stress Granule Proteins.**

99 We examined the proximal interaction networks of stress granule proteins G3BP1 and FMR1 during
100 oxidative stress. Previously, we reported that the proximal interactions of G3BP1 and EIF4A1 remained
101 largely unchanged before and after stress granule formation when using the slow biotin ligase BirA* [51].
102 However, this approach involved a labeling period significantly longer than the known kinetics of stress
103 granule formation. To capture these interactions more accurately, we employed the faster biotin ligase,

104 miniTurbo[52], which enables proximal labeling within 15~30 minutes, compared to the 3–24 hours required
105 by BirA*. We integrated expression constructs of G3BP1 and FMR1, each fused to miniTurbo-3xFLAG
106 (miniT), into the inducible Flp-In locus T-Rex HEK293 system. The expression levels of miniT-tagged
107 proteins were comparable to their endogenous counterparts (Figure S1A), increasing total protein
108 abundance by about two-fold. Since G3BP1 is known to scaffold stress granule condensation, we checked
109 for stress granule formation without stress and found no stress granules in untreated cells (Figure S1B).
110 To assess proximal interaction changes upon stress granule assembly, we induced bait protein
111 expression in biotin-depleted media and pulse-labeled for 30 min in either steady state condition (T1) or 5
112 min into oxidative stress induced with 0.5mM sodium arsenite (T2; Figure 1A; see Methods). Proteins
113 biotinylated during T1 displayed a general cytoplasmic distribution, whereas, during T2, they were highly
114 enriched in cytosolic puncta, colocalizing with the stress granule marker TIAR (Figure S1B).
115 Biological duplicates of G3BP1, FMR1, and negative controls (miniT alone, miniT-GFP, and parental
116 cells) were processed for BioID coupled to mass spectrometry (MS) followed by SAINTexpress analysis[53,54]
117 to determine high-confidence proximal interactors (BFDR ≤0.05). G3BP1 and FMR1 identified 137 and 102
118 high-confidence interactors at steady state and 107 and 139 during stress, respectively (Table S1, BFDR
119 ≤0.05). The steady-state interactors showed substantial overlap with published BirA* data, recovering 80%
120 (57/71) for G3BP1 and 68% (51/75) for FMR1 while also identifying 80 and 51 novel interactors,
121 respectively.
122 Although most proximal interactors remained similar in abundance as reported[51,55], the improved
123 labeling kinetics of the miniTurbo enzyme revealed a higher fraction of interactors displaying stress-
124 dependent abundance changes. Approximately 4% and 30% of G3BP1 interactors, as well as 34% and
125 15% of FMR1 interactors, displayed ≥1.5-fold increase or decrease in abundance, respectively (Figure 1B).
126 Common changes in G3BP1 and FMR1's stress BioID profiles included shared increased interactors (*e.g.,*
127 BICC1, TRIM56) and decreased interactors (*e.g.,* CNOT1, CNOT2, CNOT3, CNOT4). These findings
128 indicate coordinated dynamic rearrangements in proximal interaction networks as G3BP1 and FMR1
129 condense to form stress granules.
130

131 **Stress-induced Proximal Interaction Changes Are Molecular Fingerprints of Microscopically Visible**
132 **Stress Granules.**

133 Most stress-induced changes common to G3BP1 and FMR1 are abundance changes (~1.5~3-fold
134 changes in spectral counts) rather than their complete situational absence or presence (Figure 1B). To
135 examine if these observed abundance changes reflect dynamic molecular interactions associated with
136 stress granule formation, we repeated the BioID experiment under the stress granule-inhibiting effects of
137 lipoamide. Lipoamide is an antioxidant that blocks stress granule formation during oxidative stress by
138 preventing the oxidation of proteins[56]. This mechanism primarily acts on intrinsically disordered proteins,
139 such as SRSF1 and SFPQ, whose redox states strongly influence stress granule condensation[56].

140 Titration tests of potassium arsenate and lipoamide were used to identify effective concentrations for
141 inhibiting stress granule formation in HEK293 BioID miniT-GFP and miniT-G3BP1 cells (note that all
142 experiments involving lipoamide were used alongside potassium arsenate, a weaker oxidizer than sodium
143 arsenite). It was necessary to increase lipoamide concentration to fully inhibit stress granule formation as
144 potassium arsenate levels rose (Figure S1C). Based on these tests, cells were pre-treated with 100 μM
145 lipoamide before inducing stress with 1 mM potassium arsenate, followed by 30 min biotin labeling (Figure
146 1C). Pre-treatment with a DMSO control followed by potassium arsenate stress induced abundance
147 changes in G3BP1 proximal interactions (*e.g.,* TRIM56, BICC1, CCR4-NOT complex components; Figure
148 1C) that paralleled those seen during sodium arsenite stress (Figure 1A). However, when pre-treated with
149 lipoamide, interaction profiles remained at steady-state levels and failed to recapitulate any stress-induced
150 changes (Figure 1D). Further, lipoamide pre-treatment had no effect on G3BP1's interaction profile during
151 steady state (Figure S1D). We propose that lipoamide's modulation of the redox state of stress granule
152 proteins inhibits stress-induced changes in the G3BP1 proximal interaction network. These findings indicate
153 that the observed abundance changes in G3BP1 and FMR1's BioID profiles reflect dynamic molecular re-
154 arrangements during stress granule formation.

155

156 **Mapping the Dynamic Stress Granule Proteome During Oxidative and Hyperosmotic Stress**

157 The oxidative stress-induced changes in G3BP1's interaction profile were similarly observed during
158 FMR1 BioID. We adopted a multi-bait experimental design to extensively define the dynamic stress granule

159 proximal interaction network. Nine baits known to localize to stress granules, or their related condensates,
160 were selected with the criteria of maximizing the identification of stress granule proteins. Combining these
161 baits (CELF1, DAZL, CNOT2, YTHDF2, ZC3HAV1, G3BP1, DDX3X, and EIF4A2, FMR1; Figure 2A; see
162 Methods) were predicted to identify 60% of high-confidence interactors from the 58 BirA*-conjugated baits
163 from the steady-state dataset[51], and 87% of the literature-curated stress granule proteome (Figure S1E,
164 Table S2). Since miniTurbioID was derived from BirA*, we anticipated similar labeling profiles.

165 As multiple molecular mechanisms support stress granule formation, we incorporated two stressors -
166 oxidative and hyperosmotic - into our BioID screens. This approach aimed to identify both conserved and
167 unique proteomic changes underlying distinct stress granule assembly pathways. Oxidative stress induces
168 stress granules by the scaffolding of key nucleator proteins (G3BP1/2) and activation of the integrated
169 stress response. Interfering with either of these, by means of knock-out (G3BP1Δ, G3BP2Δ) or loss-of-
170 function mutation (eIF2α S51A)[57,58], is sufficient to curtail stress granule formation. In contrast,
171 hyperosmotic stress does not depend on G3BP1/2 nucleators or eIF2 α phosphorylation[57-59] (Figure 2B).
172 Instead, the resulting cellular crowding during hyperosmotic stress drives stress granule nucleation[60,61].

173 Accordingly, we performed separate BioID time course experiments to measure the dynamic
174 rearrangement of the stress granule proximal interaction network during exposure and recovery from both
175 stressors. We labelled cells 5 min into oxidative stress for 30 minutes (T2_AS; AS = arsenite) and 1hr after
176 recovering from oxidative stress (T3_AS) based on our estimate of dissolution kinetics (Figure S2A) and
177 published report[62]. For hyperosmotic stress, we noted small stress granules forming upon exposure to 0.2M
178 NaCl, with growth observed up to 45 minutes into stress (Figure S2B). We observe robust
179 eIF2α phosphorylation upon 30 minutes of exposure to oxidative stress and a moderate increase after 60
180 minutes of hyperosmotic stress (Figure S2C). Biotin labeling commenced 45 minutes into NaCl stress for
181 30min (T2_NaCl), and we confirmed the enrichment of biotinylated proteins in NaCl-induced stress granules
182 (Figure S2D). Upon removal of hyperosmotic stress, stress granules rapidly disassembled (Figure S2E).
183 Consequently, we initiated biotin labeling immediately after hyperosmotic stress removal (T3_NaCl; Figure
184 S2F). The differences in disassembly kinetics between oxidative (AS) and hyperosmotic (NaCl) stress
185 correlated with faster translational resumption following hyperosmotic stress recovery (Figure S2G).

186 Nine stress granule, stress granule/P-body baits, stably and inducibly expressed in HEK293 cells,
187 underwent 30 minutes of biotin pulse labelling at various time points (T1-3) under oxidative (AS) or
188 hyperosmotic (NaCl) stress (Figure 2B, Figure S2F), with two biological replicates for each experiment. In
189 total, we collected 108 BioID samples plus 34 negative controls, including miniT or minT-GFP labeling
190 during each stress time course to represent non-specific labelling and parental cells without miniT to capture
191 endogenously biotinylated species (Figure S3A). BioID samples were processed and analyzed using
192 conventional data-dependent acquisition (DDA) in the mass spectrometer, followed by SAINT analysis.
193 This identified 5,605 high-confidence proximal interactions across 45 bait-stress conditions and 754 preys
194 (BFDR $\leq$ 0.05 SAINTexpress, Table S3). DDA analysis of the nine baits at steady-state recovered ~40% of
195 high-confidence interactors reported in BirA* dataset. Importantly, 312 novel interactors were identified
196 throughout the stress time course [51] (Figure 2C). High-confidence interactors were significantly enriched
197 for Gene Ontology (GO) terms related to stress granules (cytoplasmic stress granule; GO:0010494, mRNA
198 binding; GO:0003729, translation; GO:0006412), though also for microtubule-related terms, including
199 microtubule organizing center (GO:0005815) and microtubule cytoskeleton (GO: 0015630) (Table S3). The
200 significance of microtubules and motor proteins in stress granule formation has been previously
201 documented for stress granules induced by oxidative stress[63,64]. However, in this dataset, proximal
202 interactions with microtubule proteins were encountered specifically during the T2_NaCl timepoint (Figure
203 S3B).
204 To see if these interactions with microtubule-associated proteins are unique to "mature" stress granules
205 formed later in stress, we performed BioID in DDX3X-miniT at an earlier time point (5-35 min post-NaCl
206 exposure) and found similar results. These interactions were reproduced during hyperosmotic stress
207 induced by sorbitol (0.4M) (Figure S3C, Table S3), indicating that DDX3X's increased association with
208 microtubule and centrosome proteins is a general response to hyperosmotic stress. To assess whether
209 these interactions were a non-specific result of hyperosmotic stress mediated-molecular crowding, we
210 examined the proximal interactions of the P-body marker DCP1A. However, increased interactions with
211 microtubule-associated proteins were not identified by DCP1A, suggesting this change is unique to stress
212 granule baits (Figure S3D, Table S3).
213

Quantitative Analysis of Stress BioID Reveals Context-Specific Rewiring of Proximal Interaction Networks During Stress Granule Condensation and Dissolution

A. Identification of High-Confident Interactions using SAINTq

Under the DDA-based analytical framework, a large portion of the dataset was marked by missing values across different stress time points. Intensity-based quantifications for 33% of high-confidence preys were absent in over 80% of bait-condition pairs. The high incidence of missing values likely stemmed from the semi-stochastic nature of DDA mass spectrometry, which opts for simple, accurate peptide identification at the cost of a selection bias for highly abundant peptides during the MS1 scan (Figure S4A).

To improve the quantitative analysis, we re-analyzed our BioID samples using data-independent acquisition (DIA) mass spectrometry, which scans all precursor ions within sliding m/z windows, thus improving sensitivity and reducing missing values[65] (Figure S4A). We built a DIA analysis workflow tailored to BioID samples to accommodate the frequent variability in interactor abundance and identity among different baits (Figure S4B, Figure 2D). In brief, DIA output was deconvoluted with DIA-NN[66] for protein identification and quantification, analyzed with SAINTq[67] to define high-confidence interactors, and with ANOVA and a post hoc Tukey's test, we identified significant quantitative changes (see Methods).

Overall, DIA improved detection sensitivity, resulting in a ~two-fold increase in protein identification across all BioID experiments prior to SAINTq analysis (Figure S4C). It also improved data completeness, reducing the proportion of missing values from 33% to 8% across 80% or more of the bait-condition pairs, as measured by Jaccard index (Figure S2D). After SAINTq analysis, we identified over 2,000 novel interactors compared to previously reported stress granule datasets generated using proximity-dependent biotinylation techniques (Figure S4E).

Next, we compared high-confidence interactors (BFDR $\leq$ 0.03, SAINTq) identified in steady state (T1) against those in oxidative (T2_AS) or hyperosmotic stress (T2_NaCl) (Figure 2E). Following oxidative stress, 472 out of 1290 (35%) T1 interactors no longer registered as statistically significant, though 225 interactors were newly identified in the T2_AS condition (≥1 bait). In contrast, under hyperosmotic stress, there was only a marginal loss of T1 interactors, however, this was accompanied by a two-fold increase in high-confidence T2_NaCl interactors (≥1 bait). These results indicate a stress-specific component to the dynamic rearrangement of the stress granule proximal interaction network.

242 To accurately discern stress granule-revelant interactions, we filtered for high-confidence interactors
243 recorded by multiple stress granule baits (BFDR ≤ 0.03; ≥ 2 baits). Under these criteria, DIA-SAINTq
244 analysis identified 13,836 high-confidence bait-prey interactions across the entire BioID dataset, comprising
245 1,801 unique preys (Table S4). This yields a bait-specific recovery rate of 10-64% of the protein-protein
246 interactions annotated in BioGRID, with stress time points observing marginally greater recovery (Table
247 S4).

248 The BioID data is well visualized by hierarchical clustering analysis of the bait-condition and prey
249 abundance matrix (Figure 2F; see Methods). Bait-condition combinations primarily clustered according to
250 bait protein, rather than stress condition, indicating that each bait maintains a distinct labeling profile
251 regardless of state changes. However, all baits (except CNOT2) resolve into two distinct clusters during
252 hyperosmotic stress (gray boxes 1 and 2 in Figure 2F). This clustering of T2_NaCl samples is attributed to
253 proximal interactors exhibiting greater abundances (red box) compared to their T1, T2_AS, or T3 sample
254 analogs (black box; Figure 2F).

255 High-confidence preys cluster into four large groups characterized by distinct GO term enrichment
256 (Figure 2G, Table S5). Cluster 3 preys are most abundant and comprise known stress granule components.
257 Expectedly, these are enriched for terms including "cytoplasmic ribonucleoprotein granule" (GO:0036464)
258 and "stress granule assembly" (GO:0034063). Cluster 1 is similarly defined by GO terms relevant to stress
259 granule biology, such as "mRNA 3' UTR binding" (GO:0003730), but also unexpected terms like
260 "cytoplasmic large ribosomal subunit" (GO:0022625). An enrichment for proteins associated with the
261 "microtubule cytoskeleton" (GO:0015630) and those presenting "kinase activity" (GO:0016301) are found
262 in cluster 2. Preys in this cluster are detected at a higher abundance in T2_NaCl samples. Finally, cluster
263 4 shows enrichment for proteins in the "cytoskeleton" (GO:0005856) and "mRNA 3'-UTR AU-rich region
264 binding" (GO:0035925). Many unanticipated GO terms belong to hyperosmotic stress-specific interactors,
265 highlighting the context-specific nature of the stress granule proximal interaction network.

266 ***B. Measuring Stress-Induced Quantitative Changes Using ANOVA***

267 Using the intensity-based quantitative values measured by DIA analysis, we sought to identify significant
268 changes in the abundance of high-confidence interactors throughout the stress time course. Quantitative
269 changes in proximal interactions between all time points (T1 *vs.* T2, T2 *vs.* T3, T1 *vs.* T3) were assessed

270 using a linear mixed model ANOVA with Tukey post hoc test (Figure 2C, Figure S4B, Methods). We
271 analyzed 22,899 and high-confidence bait-prey interactions during oxidative and hyperosmotic stress
272 transitions, respectively (preys identified with BFDR $\leq$ 0.03 in any given time point for each stress condition).
273 Significant changes were identified in 869 (3.8%) and 4,881 (21%) bait-prey pairs during oxidative and
274 hyperosmotic stress and recovery transitions, respectively ($\geq$ 1.5-fold intensity change; ANOVA with Tukey
275 post hoc test p-value$_{adj}$ $\leq$ 0.01).

276 Despite the apparent increase in protein concentration within stress granules, contrary to our
277 expectations, high-confidence prey abundance remained largely unchanged following exposure to oxidative
278 stress (Figure S4F). In contrast, the corresponding distribution tended toward positive fold-change during
279 hyperosmotic stress (Figure S4F). Interactions that increased during hyperosmotic stress would later return
280 to steady-state levels, as indicated by the negative fold-changes observed during the transition from stress
281 to recovery. These increased interactions during hyperosmotic stress were specific to high-confidence
282 interactors, with the overall intensity of non-significant interactions remaining similar between stress and
283 steady state (median fold-change for non-significant interactors: 1.05 *vs.* high-confidence interactors: 1.27).
284 This suggests increases in stress granule-specific interactions rather than as a result of general
285 overcrowding in the cytoplasmic space.

286 ***C. Validation of Identified Stress-Specific Interactors***

287 We selected several proteins that increased in a stress-specific manner during stress granule formation
288 for colocalization analysis with the stress granule marker G3BP1. TRIM56, BICC1, LARP6, and NYNRIN
289 increased in abundance during oxidative stress, but remained unchanged during hyperosmotic stress.
290 Colocalization analysis was performed under both stress conditions using antibodies against endogenous
291 proteins and HeLa cells stably expressing mCherry-tagged proteins. All tested preys localized to stress
292 granules regardless of the inducing agent, except for TRIM56, whose recruitment to stress granules was
293 specific to oxidative stress (Figure S4G; data not shown). BICC1, LARP6, and NYNRIN's localization to
294 stress granules during hyperosmotic stress, despite their unchanged abundance measurements, is not
295 unexpected, as the majority of known stress granule proteins displayed minimal changes in abundance
296 under either stress condition. We further investigated if TRIM56 plays a role in stress granule formation.
297 The loss of TRIM56 through CRISPR-mediated knock-out did not affect stress granule formation capacity,

298 indicating that increased association with specific components does not entail their essentiality for stress
299 granule formation (data not shown).
300 Additionally, a strong enrichment for centrosome-associated proteins was observed during
301 hyperosmotic stress. However, colocalization analysis of a subset of these centrosome-associated proteins
302 (CEP170B, PCNT and CEP192) during hyperosmotic stress revealed poor enrichment within stress
303 granules (data not shown). This data suggests that the proximal interactions with centrosome-associated
304 proteins might be occurring in the dilute phase or submicroscopic stress granules.
305
306 **Dynamic Proximal Interactions with the CCR4-NOT Deadenylase Complex is Universal during**
307 **Stress Granule Assembly**
308 We hypothesized that quantitative changes across multiple baits would reflect compositional alterations
309 at the condensate level, and those common to both stressors could help identify a shared mechanism
310 underlying stress granule formation. To assess condensate-level changes for each stress, proximal
311 interactions were filtered for high-confidence preys demonstrating consistent trends in their interaction
312 changes (≥ 1.5-fold increase, decrease or unchanged) across two or more baits (Table S6). Consistent
313 changes were observed during hyperosmotic stress (n=564) and oxidative stress (n=68).
314 Next, we assessed shared changes in abundance in both stressors (Figure 2H). While only two high-
315 confidence preys (SUGT, DLD) increased in both oxidative and hyperosmotic stress (≥1.5-fold; ≥2 baits),
316 a significant amount of overlap was observed among interactors that consistently decreased in abundance
317 (30% and 48% of decreasing preys in hyperosmotic and oxidative stress, respectively). These included
318 RNA-binding proteins involved in mRNA deadenylation, translation repression and mRNA decay (*e.g.,*
319 CCR4-NOT complex components and interactors, including TOB1, EIF4E2, and EIF4ENIF1).
320 GO term enrichment analysis of interactors that shift in abundance during stress and recovery (Table
321 S6) identified terms related to 'CCR4-NOT deadenylase complex' among preys that decrease during stress
322 granules formation and later increase as they disassemble. This trend is consistent across both conditions,
323 as evidenced by the quantitative changes in G3BP1 proximal interactors (Figure S4H). Notably, the
324 decreased association with CCR4-NOT components from T1 to T2 quickly recovers during the T2 to T3
325 transition (Table S6). No changes in total protein abundance of the CCR4-NOT components were observed

326 (data not shown). Together, these observations show the coupling of CCR4-NOT proximal interactions with
327 stress granule assembly dynamics, implicating stress granule formation as a possible regulatory
328 mechanism controlling mRNA deadenylation and translation repression.
329
330 **Loss of the CCR4-NOT Deadenylase Complex Blocks Lipoamide-induced Inhibition of Stress**
331 **Granule Condensation.**
332 As stated, pre-treatment with lipoamide effectively inhibits stress granule formation (Figure 1C). To
333 further characterize this inhibitory pathway and elucidate mechanisms regulating stress granule formation,
334 we performed a genome-wide CRISPR-Cas9-mediated gene knockout screen (Figure 3A). HeLa cells
335 stably expressing Cas9 and single guide RNAs (sgRNAs) were pre-treated with lipoamide prior to stress
336 with potassium arsenate. Confocal images of stress granules, identified by punctate forms of stably
337 expressed FUS::GFP signals, were segmented, quantified, normalized, and transformed into z-scores
338 (Figure 3B; Methods). Notably, the knockout of SRSF1 abolished the inhibitory effects of lipoamide (z-score
339 = 17.5; Figure 3B). This result substantiates the screen, as SRSF1 has previously been shown to prevent
340 lipoamide activity on stress granules[56]. Other gene knockouts (*e.g.,* SLC3A2, ABCC1, RPLs - large
341 ribosomal subunits, and PPIP5K2) also produced similar inhibitory effects (Figure 3B, Table S7).
342 The microscopy data was manually reviewed, and 81 genes were selected for further validation using
343 endoribonuclease-prepared small interfering RNA (esiRNA)-mediated gene knockdown. Using the same
344 experimental workflow and analysis pipeline as the primary screen, we observed candidates that robustly
345 induced stress granule formation in cells pre-treated with lipoamide (Table S7; Figure 3C). Examination of
346 stress granule dynamics in the absence of lipoamide, arsenate, or both revealed that the depletion of 22
347 genes induced constitutive stress granule formation (filled in gray, Fig 3D; Table S7). These genes,
348 including those that encode for helicases, exosome components, ribosome components, and components
349 involved in ribosome biogenesis (RNA polymerase I and WDR43), induced cytosolic FUS::GFP puncta in
350 the absence of cellular stress. Excluding these genes, the depletion of nine others effectively blocked the
351 inhibitory effect of lipoamide on stress granule formation, including our positive control, SRSF1 (genes in
352 boxes; Figure 3D; Table S7).

353 Among these, GCLC and SLC3A2 are involved in glutathione biosynthesis[68], supporting the redox-
354 associated role of lipoamide for stress granule dynamics[56]. Additionally, the proteasome subunits like
355 PSMA6 and PSMD7 were validated, consistent with prior observations of proteasomal involvement in stress
356 granule dynamics[69]. Notably, PPIP5K2, a bifunctional inositol kinase, and CNOT2, a component of the
357 CCR4-NOT complex, were both identified as high-confidence interactors in our stress BioID data (Table
358 S4).

359 Given the dynamic changes in proximal associations between the CCR4-NOT complex components
360 and stress granule baits, we focused our further investigation on CNOT2. Other CCR4-NOT components
361 were depleted to determine whether CNOT2 itself or the complex plays a role in stress granule dynamics.
362 The CCR4-NOT complex consists of eleven subunits, with a conserved core formed by two major modules:
363 the NOT module (comprising the scaffolding protein CNOT1 and a CNOT2-CNOT3 heterodimer) and the
364 catalytic module (containing the deadenylase CCR4 [CNOT6, CNOT6L] and exonuclease CAF1 [CNOT7,
365 CNOT8]). The NOT module (CNOT1, CNOT2, CNOT3) is critical for maintaining complex integrity,
366 regulating the catalytic module's activity, and recruiting the complex to specific mRNAs via specific
367 interactions with RNA-binding or GW182 proteins[70-77]. Conversely, CAF1 and CCR4 modules perform the
368 deadenylase activity[43]. Depletion of the NOT module proteins abrogated lipoamide-mediated inhibition of
369 stress granule formation (Figure 3E, Table S7). However, this effect was not mirrored by the depletion of
370 the catalytic subunits CNOT7-CNOT8 and CNOT6-CNOT6L (Figure 3E). These genetic analyses
371 demonstrate that loss of the NOT module is sufficient to block the inhibitory effects of lipoamide.

372

373 **Regulation of Poly(A) Tail Lengths is Important for Stress Granule Formation.**

374 We considered two scenarios in which loss of the CCR4-NOT complex could block lipoamide's effects.
375 First, lipoamide may regulate CCR4-NOT complex function to influence stress granule formation. However,
376 previous thermal proteome profiling assays using lipoamide[56] showed no change in melting temperature
377 for CCR4-NOT complex components (CNOT1, 2, 3, 4, 6, 7, 10 and 11), advocating against their direct
378 interaction.

379 Alternatively, CCR4-NOT may operate in a parallel pathway, distinct from lipoamide regulation, to
380 promote stress granule formation. Given the established relationship between poly(A) tail length and stress

381 granule formation[49], and the broader role of mRNAs in condensate formation[78-82], we hypothesized that
382 poly(A) lengths regulated by the CCR4-NOT complex could modulate stress granule assembly. Longer
383 poly(A) tails may enhance scaffolding for stress granule formation by providing additional binding sites for
384 poly(A) binding protein (*i.e.,* PABPC1), whereas shorter poly(A) tails could diminish this ability.

385 To assess the influence of poly(A) tail shortening on stress granule formation, we utilized cordycepin,
386 an adenosine analog that inhibits polyadenylation, to reduce global poly(A) tail length[83]. Pre-treatment with
387 cordycepin prior to oxidative stress significantly reduced stress granule and P-body numbers in a
388 concentration-dependent manner (Figure 4A, B). This can be contrasted with our earlier genetic screens,
389 where inhibiting deadenylase activity by reducing the NOT module of the CCR4-NOT complex positively
390 influenced stress granule formation. Specifically, in the absence of lipoamide, the knockdown of CNOT1,
391 CNOT2, and CNOT7/8 significantly increased the number of stress granules following oxidative stress
392 (Figure 4C; Table S7). Together with prior studies reporting global poly(A) tails lengthening following the
393 loss of catalytic enzymes (CNOT7/8) and the NOT module (CNOT1 and CNOT2)[48,84,85], we propose that
394 poly(A) lengthening enhances stress granule formation.

395 We then combined siRNA-mediated knockdown of the CCR4-NOT complex with cordycepin, lipoamide
396 or both to assess whether poly(A) lengthening can counteract the stress granule-inhibitory effects of these
397 treatments during oxidative stress. While cordycepin pre-treatment alone significantly reduced stress
398 granule formation, knockdown of CNOT1 prior to acute cordycepin treatment induced stress granule
399 formation (Figure 4D). This suggests that the stimulatory effects of CCR4-NOT knockdown (*i.e.,* global
400 poly(A) lengthening) can negate the inhibitory effects of acute cordycepin treatment. However, CNOT1
401 knockdown did not overcome the combined inhibitory effects of both lipoamide and cordycepin, leading to
402 defective stress granule formation. This suggests two parallel pathways regulating stress granule formation:
403 one through redox regulation of stress granule proteins (via lipoamide) and the other through control of
404 poly(A) tail lengths (via cordycepin and CCR4-NOT activity) (Figure 4E).

405

406 **CCR4-NOT Deadenylase Complex is Sequestered to Stress Granules During Stress**

407 Components of the CCR4-NOT have been shown to co-localize with P-body markers in overexpression
408 systems[86,87]. In contrast to previous findings, we observed poor colocalization of CNOT1 with the P-body

markers EDC3 (at their endogenous levels) or with DCP1A (stably expressed under steady-state conditions) in HeLa and HEK293 Flp-In TREx cells (Figure 5A, Figure S5A). However, under both oxidative and hyperosmotic stress, CNOT1 formed large condensates adjacent to P-bodies, similar to the docking behaviour of stress granules[88]. When directly tested, CNOT1 colocalized with stress granule marker G3BP1 during both oxidative and hyperosmotic stress in HeLa and HEK293 cells (Figure 5B, Figure S5B). Other CCR4-NOT components, including the NOT module (CNOT2) and the CAF1 catalytic subunits (CNOT7 and CNOT8), localized to stress granules under these conditions in HeLa cells (Figure 5B). Additionally, stable expression of 3xFLAG epitope-tagged CNOT2 colocalized with G3BP1 in HEK293 cells (Figure S5C). Further high-resolution imaging of CNOT1 and G3BP1 during oxidative stress revealed distinct patterns of CNOT1 enrichment within the G3BP1-positive stress granules, indicating an organized partitioning into stress granule nano-compartments (Figure 5C).

Together, these findings demonstrate that in contrast to previous annotations of CCR4-NOT complex as P-body components, CCR4-NOT complex components do not localize to P-bodies at steady state and are sequestered into stress granules during cellular stress.

DISCUSSION

Biomolecular condensates are involved in a wide range of biological processes, yet their dynamic nature and lack of physical boundaries (unlike membrane organelles) pose significant challenges for study. Stress granules, a biomolecular condensate that forms in response to cellular stress, harbour thousands of mRNAs and hundreds of proteins[30,31,89]. Despite their widespread association with stress response, the precise functions of stress granules remain controversial. In this study, we leveraged multi-bait BioID profiling and quantitative mass spectrometry to provide a comprehensive resource that maps the dynamic components of stress granules proteomes. Notably, our approach integrates quantitative protein-protein interaction data with chemical genetic interaction results, known to be distinct and orthogonal in their relationships[90,91].

Our BioID profiling of stress granule-localized G3BP1 over a stress time course identified changes in proximal interactions reflecting molecular changes associated with the formation of microscopically visible stress granules (Figure 1D). Further expanding BioID profiling to nine high-information baits, we mapped dynamic proteomic landscapes of stress granules formed by distinct mechanisms (oxidative or

437 hyperosmotic stress), revealing ~2,000 novel proximal interactions previously uncharacterized in stress
438 biology and over 500 dynamic protein components (Figures 2B, 2F, 2H and S4E). Notably, these dynamic
439 proximal interactions differ significantly depending on the stress type (Figure 2E, H), indicating context-
440 specific plasticity of the stress granule proteome. Despite the stark differences in subsets of protein
441 interactions we observed, stress granule transcriptomes remain highly correlated between oxidative and
442 hyperosmotic stress[92], indicating that protein dynamics, rather than RNA, may play a more prominent role
443 in stress-specific adaptations.

444 Common to both stress conditions, the CCR4-NOT deadenylase complex and its associated proteins
445 are dynamically associated with stress granules (Figure 2H). Simultaneously, imaging-based, genome-wide
446 CRISPR screening identified nine genes that suppressed the stress granule-inhibiting effects of lipoamide.
447 These genes include CNOT2, a key component of the CCR4-NOT deadenylases complex (Figure 3D), and
448 further testing demonstrated that the loss of any NOT module protein (CNOT1, CNOT2 and CNOT3)
449 abolishes the lipoamide's inhibitory effects (Figure 3E). As the CCR4-NOT complex serves as the principal
450 deadenylase responsible for poly(A) degradation[43,48,93], we tested the effects of poly(A) tail lengths on stress
451 granule formation. Poly(A) lengthening promoted, while poly(A) shortening inhibited stress granule
452 formation (Figures 4B and 4C). We propose that loss of the NOT module circumvents lipoamide activity by
453 increasing the potential for RNA-based, condensate-forming intermolecular interactions[78,79,81,82,89] or
454 providing additional binding sites for PABPC1 through the lengthening of poly(A) tails[49] (Figure 4E).

455 Together, the dynamic rewiring of stress granule proximal interactions with the CCR4-NOT complex and
456 the effect of their loss-of-function on stress granule formation reveals a functional link between mRNA
457 deadenylation and stress granule condensation.

458 Concomitant with stress granule formation, the transcriptome's poly(A) tails lengthen globally during
459 cellular stress[44-47], but the mechanisms remain unclear. In vertebrates, poly(A) tails are primarily regulated
460 by three deadenylases: the PAN2-PAN3 complex, the CCR4-NOT complex and PARN (poly(A)-specific
461 exoribonuclease)[43]. Among these, the CCR4-NOT complex is the principal deadenylation responsible for
462 degrading poly(A)s[43,48,93]. According to a biphasic model of deadenylation, the PAN2-PAN3 complex
463 initiates the poly(A) tail removal, while the CCR4-NOT complex trims the remaining tail close to the 3'-
464 UTR[94]. To better understand stress-induced poly(A) tail lengthening, we investigated the localization of the

465 CCR4-NOT complex under stress conditions. Surprisingly, the deadenylase complex becomes
466 concentrated in stress granules during stress (Figure 5B).

467 We propose that CCR4-NOT sequestration into condensates likely inhibits the deadenylase activity of
468 the complex, leading to global poly(A) lengthening during stress (Figure 5D). Under normal cellular function,
469 the complex resides in the cytoplasm, maintaining steady-state poly(A) tail length. However, upon stress,
470 it partitions into stress granules, where its activity is regulated, analogous to how CNOT7 deadenylase
471 activity is modulated in simple FMR1-CAPRIN1 condensates *in vitro*[95]. Our findings suggest that stress
472 granules act as a depot for the deadenylase complex, thus promoting transcript stability as an adaptative
473 response to stress. Further investigation of poly(A) tails while blocking stress granule formation is essential
474 to support this model. It remains to be determined whether the complex retains enzymatic activity following
475 its localization to stress granules, potentially trimming the poly(A) tails of localized transcripts. While
476 CNOT2's proximal association with the complex members remained unchanged throughout the stress time
477 course, its proximal association with deadenylase activators, TOB1 and TOB2, was significantly reduced
478 in both stress conditions, suggesting a reduction in activity (Tables S4 and S6). Consistent with this notion,
479 nanopore sequencing of the transcriptome during stress revealed that the poly(A) tails of stress granule-
480 localized transcripts lengthen to a level comparable to those of stress granule-depleted transcripts during
481 oxidative stress[96].

482 The localization of the CCR4-NOT complex to stress granules was unexpected, given the conserved
483 reduction in its components' proximal associations with stress granule baits during stress granule formation
484 (Figure 2H). The proximal interactions measured by BioID reflect a summation of spatial interactions
485 occurring in and out of stress granules over time; in essence, they represent the cumulative effect of
486 transient and cycling interactions. We suggest that the proximal interactions between CCR4-NOT and
487 stress granule components decrease during stress due to reduced cycling interactions that accumulate
488 over time and/or the CCR4-NOT complex's partitioning to distinct stress granule nano-compartments. In
489 support of the latter, our high-resolution microscopy revealed subcompartmentalization of the CNOT1 within
490 stress granules (Figure 5C). Additionally, the CCR4-NOT complex increases its proximal association with
491 another stress granule bait protein (unpublished data), indicating bait-specific directionality in proximal
492 interaction changes.

493 In summary, our systematic mapping of dynamic proximal interaction networks in stress granules across
494 two distinct stress conditions provides a valuable resource for understanding the universal and context-
495 specific interactions underlying stress granule assembly and disassembly. Our dataset highlights the
496 versatility of stress granule interactions tailored to specific stress contexts. Through quantitative proteomics,
497 we reveal the rewiring of pre-existing proximal interactions and identify dynamic components, particularly
498 RNA-binding proteins involved in translation repression and mRNA decay, such as the CCR4-NOT
499 deadenylase complex. By integrating proteomics with chemical genetics, we further elucidate the
500 mechanisms underlying stress granule formation via poly(A) tail regulation. Notably, in contrast to previous
501 findings, we show that the CCR4-NOT complex is not localized to P-bodies, but is instead a dynamic
502 component of stress granules. Recognizing stress-responsive biomolecular condensates as key
503 mechanisms for stress adaptation[97-99], we propose that stress granule condensation is functionally coupled
504 to transcriptome stabilization through the regulated sequestration of CCR4-NOT.
505

506 **LIMITATIONS OF THIS STUDY**

507 We report dynamic proximal interaction profiles of multiple stress granule proteins utilized as molecular
508 probes for stress granule condensate. While we are confident of proximal associations reported here, we
509 cannot discern where these proximal interactions occur (*i.e.,* inside or outside microscopically visible stress
510 granules). Thus, further analysis and experimentation are required to determine context-specific stress
511 granule proteome. As with any screening approach, our proteomics and genetic screening methods contain
512 false negatives.
513

514 **METHODS**

515 **Cell culture and stable cell line generation**

516 HEK293 Flp-In T-REx (Invitrogen, R780-07; used for fixed-cell microscopy and BioID experiments),
517 HeLa Flp-In T-Rex (Arshad Desai Lab), and HeLa (Anne-Claude Gingras Lab) cells were grown at 37ºC in
518 DMEM high glucose media supplemented with 5% Fetal Bovine Serum (FBS), 5% cosmic calf serum, and
519 100 U/mL penicillin/streptomycin (growth media). Cells were regularly passaged upon attaining 80-100%
520 confluency and monitored for mycoplasma contamination.

521 All expression constructs were created using Gateway LR cloning (Thermo Fischer). Entry clones for
522 each bait protein were recombined with a destination vector (pDEST-3xFLAG-miniTurbo for BioID and
523 pDEST-mCherry for microscopy-based assays, gifts from Anne-Claude Gingras, Lunenfeld-Tanenbaum
524 Research Institute) to obtain expression constructs.
525 To generate stable cell lines, our expression constructs were transfected into Flp-In T-Rex parental cells
526 following a modified jetPRIME® protocol (Polyplus, CA89129-924). Briefly, cells were seeded at 25~30%
527 confluency in a 6-well plate. The following day, cells were transfected with a mixture of 1 µg pOG44 DNA,
528 100 ng bait construct DNA, and 2 µL jetPRIME reagent in 200 µL jetPRIME buffer (day 2). On day 3, cells
529 were passaged to 10 cm dishes and grown to 80% confluency, where successful transfectants were
530 selected for using Hygromycin B-supplemented growth media (200 ug/mL; Wisent, 450-141-XL) starting on
531 day 4. Selection media was changed every 2-3 days, until clonal colonies were visible; clonal colonies were
532 pooled together to generate stable cell lines.
533
534 **Stress BioID sample preparation**
535 HEK293 Flp-In T-REx cell lines stably, inducibly expressing BioID constructs, and negative control cell
536 lines (miniT-GFP and HEK293 parental line) were seeded into 10 cm dishes at 30% confluency in 10 mL
537 growth media. After 24 hrs, protein expression was induced with tetracycline (1 µg/mL) in biotin-depleted
538 growth media for 20 hrs. Biotin-depleted media is standard growth media prepared with biotin-depleted
539 FBS and cosmic calf serum (as reported in Schreiber *et al.,* 2024[100]). Biotin labeling was then performed
540 for 30 mins using growth media supplemented with 50 µM biotin in (1) untreated cells, (2) stress-treated
541 cells, and (3) stress-recovering cells. Stress, recovery, and labelling timelines follow the steps summarized
542 in Figure S2C. For alternative NaCl stress timepoint (T2; 5'-35'), biotin labeling began 5 min into 0.2M NaCl
543 stress for 30min following the same regime as oxidative (AS) stress and recovery timepoint (T3; 35'-65'),
544 biotin labeling was performed concomitantly with fresh media change after 35' of 0.2M NaCl stress (Figure
545 S3C). For lipoamide stress BioID, bait expression was induced for 24hr in biotin-depleted media. Next day,
546 cells were pre-treated with either DMSO (carrier) or 100 µM lipoamide for 1hr prior, then exposed to 1mM
547 or 0mM of potassium arsenate for 1hr, after which 50 µM biotin was added for 30min of labelling. After
548 labelling, cells were rinsed with phosphate-buffered saline (PBS) and lifted using 0.05% trypsin. Harvested

549 cells were rinsed with PBS, transferred to pre-weighed 1.5 mL Eppendorf tubes, pelleted, and flash frozen
550 on dry ice and stored at -80ºC.
551
552 **Immunofluorescence (IF) microscopy**
553 For bait localization and prey colocalization tests, stable HEK293 or HeLa Flp-In T-Rex BioID cell lines
554 were seeded onto glass coverslips in 6-well plates at 20% confluency in 2 mL growth media, and protein
555 expression was induced after 24 hrs with tetracycline (1 µg/mL) for 20 hrs. For lipoamide titration test,
556 HEK293 BioID stable cells stably expressing miniT-G3BP1 or miniT-GFP were seeded at 30% confluency,
557 then induced for bait expression for 24 hrs. The next day, varying concentration of lipoamide (0-100 uM) or
558 carrier (DMSO) was added, followed by no treatment (untreated) or potassium arsenite stress (1 – 2 mM).
559 For stress granule formation assays in cordyceptin treatment (Figure 4A-B), HEK293 Flp-In T-Rex, HeLa
560 Flp-In T-Rex, or HeLa cells were seeded onto glass coverslips in growth media. Glass coverslips were
561 treated with poly-D-lysine for 1 hour at 37 degrees prior to seeding HEK293 Flp-In T-Rex cells. Cells
562 reached 90% confluency 24-48 hours post seeding onto the glass coverslips and were treated with either
563 a media change (untreated), sodium arsenite [60 uM – 1 hour, 75 uM – 1 hour, 500 uM – 30 mins], sodium
564 chloride [0.2 M – 1 hour], or sorbitol [sorb: 0.4 M, 1 hr]) at 37ºC. For the cordycepin treatment in Figure 4A-
565 B, cells were pretreated with varying concentrations of cordycepin [0-100 uM; C3394, Sigma-Aldrich] for
566 three hours, with varying amounts of sodium arsenite added during the last hour before fixation. For the
567 cordycepin treatment in Figure 4D, the HeLa Kyoto FUS::GFP cells were first treated with the indicated
568 concentration of cordycepin (C2689, Tokyo Chemical Industry) for 1 h, then treated with 10 µM of lipoamide
569 or the corresponding percentage (v/v) of DMSO (0.1%) as the control for 1 h, and finally stressed with 1 mM
570 of potassium arsenate for 1 h before fixed with 4% formaldehyde in PBS.
571 Cells were processed for IF immediately following drug treatments by rinsing the cells with PBS twice,
572 then fixing with 4% paraformaldehyde in PBS for 10-15 minutes. Post fixation, cells were washed 3 times
573 with PBS or TBS-T and then permeabilized with -20ºC Methanol (Figure 4A, Figure 5, S2B, S5A-B) or 0.1%
574 Triton-X in TBS-T (Figure 1B, S2A, S2D, S2E, S4F, S5C) at for 10 minutes. Cells were then washed 3
575 times with PBS or TBS-T, then blocked with 5% milk in TBS-T or 5% BSA in PBS for 1 hour. Coverslips
576 were then incubated in primary antibody solution prepared in 5% BSA in PBS for 1 hour or overnight

577 (depending on the antibody) in a humidity chamber at 4 degrees. The cells were then washed 3 times with
578 PBS or TBS-T and then incubated with secondary antibodies and DAPI prepared in 5% BSA or milk blocking
579 solution for 1 hour in the dark. Coverslips were then washed for 3 times with PBS or TBS-T. Finally, samples
580 were mounted onto slides using Prolong Gold and cured in the dark overnight. All steps were performed at
581 room temperature excluding the overnight incubation. See Table 1 for a list of antibodies used in all fixed-
582 cell imaging experiments. Samples were imaged using the Leica SP8 Confocal Microscope and the Leica
583 Stellaris 5 Confocal Microscope at 40X and/or 63X magnification, and images were processed using either
584 IMARIS or LASX software.
585
586 **Puromycin Incorporation Assay**
587 HEK293 Flp-In TREx cells were plated on a 6-well plate. For each time point, puromycin was incubated
588 for 10 min at a final concentration of 10ug/ml, as described in Schmidt *et al.*[101]. Cells were either untreated,
589 stressed, or stressed then recovered and puromycin incorporation was performed at indicated condition
590 and timeframes in Figure S2G. Cells were then lifted using trypsin and collected in pre-weighed centrifuge
591 tubes. Cells were normalized by pellet weight and lysed with 2% SDS in Tris-HCL pH 7.5. Samples were
592 boiled with Laemmli sample buffer for 5 minutes at 95 ºC, then analyzed by Western blot (Puromycin
593 Antibody, clone 12D10, Sigma, MABE343).
594
595 **BioID bait selection process**
596 Bait proteins were selected for BioID experimentation by optimizing for the maximum number of
597 theoretical bait-prey interactions using published steady state BirA* BioID data[51]. We found that 58 baits
598 profiled in steady state data showed high specificity in their ability to label and identify literature-curated
599 RNA granule proteins (*i.e.,* ≥70% of their high-confidence interactors are annotated as Tier 1[102]). Using the
600 concepts of the greedy heuristic, we predicted that using five baits (DAZL, YTHDF2, DDX3X, CNOT2,
601 EIF4A2) would recover ~75% of the literature-curated Tier 1 stress granule proteome[102]. The previous study
602 identified stress granule proteins that dually localize to stress granules and other compartments, like P-
603 bodies and nuclear ribonucleoprotein (RNP) complex[51]. To capture components that dynamically transit
604 between stress granules and other RNA-containing compartments, we included CELF1 and ZC3HAV1,

605 which identify stress granule proteins and proteins in the nuclear RNP complex or P-bodies, respectively.
606 Next, G3BP1 and FMR1 were added for their importance in stress granule dynamics and translation
607 regulation, respectively. The final list and their relevant selection criteria are summarized in Table S1.
608
609 **BioID sample purification for mass spectrometry**
610 Cell pellets were thawed and resuspended in ice-cold modified RIPA lysis buffer (50 mM Tris-HCl [pH
611 7.5], 150 mM NaCl, 1 mM EGTA, 1.5 mM MgCl2, 1% NP-40, 0.1% SDS) + protease inhibitor cocktail at a
612 1:10 milligram-to-millilitre ratio. Samples were sonicated for 30 s (10 s on, 5 s off, repeat x3) at 30%
613 amplitude using a 1/8" microtip at 4ºC. 250 U of Benzonase Nuclease was added to each sample, which
614 was then rotated end-over-end for 15 mins at 4ºC. Sample SDS concentration was raised to 0.4%, then
615 rotated end-over-end for 5 mins at 4ºC. Lysate volume was normalized to the lowest weight sample within
616 a bait-stress group, then centrifuged at 20,000 g for 20 mins at 4ºC. Lysates were added to 15 µL of modified
617 RIPA-washed Streptavidin-Sepharose beads of ~60% slurry, then rotated end-over-end for 3 hrs at 4ºC.
618 Beads were pelleted by centrifugation at 500 g for 1 min, the supernatant aspirated, and the beads
619 transferred to a new 1.5 mL Eppendorf tube using 1 mL modified RIPA buffer. Next, beads were subject to
620 consecutive 1 mL washes (1 x SDS wash (50mM Tris-HCl [pH 7.5]), 2 x modified RIPA washes, 3 x
621 ammonium bicarbonate (ABC) washes (200 mM ABC)), pelleting and aspirating off wash solutions in
622 between. Beads were resuspended in 1 µg trypsin in 30 µL of 50 mM ABC solution for overnight on-bead
623 digestion at 37ºC with agitation. The next day (16 hours after trypsin addition), 0.5 µg trypsin in 10 µL of 50
624 mM ABC was added to each sample, allowing the samples to digest for a further 3.5 hours at 37ºC. Beads
625 were pelleted by centrifugation at 400 g for 2 mins, the supernatants containing released peptides were
626 collected into a final collection tube, and the beads were washed with high-performance liquid
627 chromatography (HPLC)-grade water twice, pelleting the beads and collecting the supernatants into the
628 final collection tubes each time. The final collection tubes, carrying the total peptide supernatants, were
629 centrifuged at 16,100 g for 10 mins, and the top 80 µL was transferred to new tubes, which were acidified
630 to 2% formic acid to stop tryptic digestion and dried down in a centrifugal vacuum concentrator.
631
632 **Liquid Chromatography-Mass Spectrometry**

633 BioID peptides were resuspended in 12 µL of 5% formic acid and centrifuged at >20,000 x g for 1 min.
634 For MS analysis of BioID peptides, each sample was further normalized to the smallest pellet weight across
635 all bait-stress groups by diluting ~1-2 µL of the peptide solution with 5% formic acid to a volume of 12 µL.
636 Subsequently, 1 µL of 50 fmol/mL Pierce Retention Time Calibration (iRT) peptides was added, bringing
637 the final volume to 13 µL.

638 For each sample, 6 µL of peptides was loaded onto a 10.5 cm 75 µm ID emitter tip packed in-house with
639 3 µm ReproSil Gold 120 C18 (Dr. Maisch HPLC GmbH) using an Easy-nLC 1200 liquid chromatography
640 system. Peptides were eluted at 200 nL/min over a 120 min gradient, starting with 2.4% acetonitrile in 0.1%
641 formic acid and gradually increasing to 35% acetonitrile. The acetonitrile concentration was further
642 increased to 80% over an 8 min gradient and maintained at this concentration for 16 min at 200 nL/min, for
643 a total run time of 144 min. Samples were analyzed with an Orbitrap Exploris 480 (Thermo Fisher Scientific)
644 in both Data-Independent Acquisition and Data-Dependent Acquisition modes. Instrument
645 conFigureurations for both acquisition modes were set up using Thermo Xcalibur software. The instrument
646 was operated with a positive polarity ion voltage of 2.4 kV and the ion transfer tube temperature was set to
647 300 °C. MS analyses of each BioID sample was done in both DIA and DDA modes consecutively, while the
648 fractionated HEK293 peptides were analyzed in DDA mode only.

649 For DDA experiments, MS1 scans ranged from 390-1010 m/z were performed at a resolution of 120,000,
650 with a 3-second cycle time. The normalized automatic gain control (AGC) target was set to 125%. Precursor
651 ions with charges from 2+ to 7+ that exceeded an intensity threshold of 1.0×10^3 were selected for
652 fragmentation with dynamic exclusion enabled for 9 seconds. Fragmentation was achieved with a
653 normalized collision energy (NCE) of 33%. MS2 scans were performed at a resolution of 15,000, with a
654 normalized ACG target of 400%, and a maximum injection time of 50 ms.

655 For DIA experiments, a staggered window scheme was utilized as described in detailed in Pino *et al.*,
656 2020[103]. Briefly, this approach employed two alternating precursor isolation patterns with the m/z ranges of
657 400-1,000 and 396-1,004 m/z, respectively. Each set had an 8 *m/z* precursor isolation window at a 15,000
658 resolution, with a scan range of 145-1450 m/z, a normalized ACG target of 1000%, and a maximum injection
659 time of 23 ms. The full scan range was set to 390-1,010 m/z at a resolution of 60,000, with a normalized

660 ACG target of 100%, and a maximum injection time of 55 ms. NCE of 33% was used for precursor
661 fragmentation.
662
663 **Mass Spectrometry Data Analysis (Data-Dependent Acquisition) and Spectral Library Generation**
664 All MS Thermo RAW files acquired in DDA mode were analyzed with FragPipe (v20.0), MSFragger
665 (v3.8), IonQuant (v1.9.8) and Philosopher (v5.0.0). The protein sequence database contains reviewed
666 UniProt entries and 15 iRT peptides as well as the same number of reversed decoy sequences, with a total
667 search space of 40,884 sequences. The precursor mass window was set at ±20ppm and the fragment
668 mass tolerance was set at ±20ppm. Methionine oxidation, and N-terminal acetylation were set as variable
669 modifications. Additionally, peptide N-terminus heavy arginine (+10.008269) and heavy lysine (+8.014199)
670 were included as variable modifications to facilitate the identification of iRT peptides. MSBooster was
671 enabled, which uses deep learning to predict retention time and spectra to increase identifications[104]. PSM
672 validation was done using Percolator (--only-psm --no-terminate --post-processing-tdc), which uses a linear
673 support vector to performs FDR calculations using a target-decoy approach[105]. This is followed by protein
674 inference by ProteinProphet (--maxppmdiff 20)[106]. FDR filtering was done using Philosopher to 1% PSM
675 and protein levels (--sequential --picked --prot 0.01).
676 MS1 intensity-based quantification was conducted using IonQuant with Match-Between-Runs
677 (MBR) enabled (default parameters)[107,108]. MaxLFQ intensity (with minimum ions set to 2) was used for
678 downstream statistical analysis. For feature detection and peak tracing, m/z tolerance was set to 10ppm
679 and RT Window to 0.6. MBR top runs was set to 10.
680 The DDA search results from fractionated peptides of HEK293 lysate and BioID peptides were
681 compiled into a spectral library using EasyPQP with default parameters (v0.1.42)
682 (https://github.com/grosenberger/easypqp). Finally, the six most intense fragments were selected for each
683 precursor to generate the spectral library for DIA MS analysis[109]. The final spectral library contains 193,510
684 precursors from 9,860 proteins.
685
686 **Mass Spectrometry Data Analysis (Data-Independent Acquisition)**

687 DIA-MS data acquired using the staggered window scheme require a computational demultiplexing step
688 before they can be processed by data analysis softwares. This step separates the 8 m/z staggered
689 precursor isolation windows into 4 *m*/*z* effective windows such that the converted mzML output file contains
690 isolation windows 400–404 *m*/*z*, 404–408 *m*/*z*, 408–412 *m*/*z*, etc. The demultiplexing was performed by
691 MSConvert (Proteomewizard) with the following filters: 1) "*peakpicking vendor msLevel=1-*"; 2) "*demultiplex*
692 *optimization=overlap_only massError=10.0ppm*". Following the file conversion, the mzML files were
693 analyzed by the DIA-NN software (v1.8.1) using a library-based approach. DIA-NN was conFigured with
694 match-between-runs enabled, and cross-run normalization disabled. Additionally, the *"--report-lib-info*" flag
695 was set to generate fragment-level intensity values in the resulting report.tsv file, which was used for
696 downstream statistical analysis.
697
698 **Mass Spectrometry Data Deposition**
699 Datasets consisting of raw files and associated peak list and results files have been deposited in
700 ProteomeXchange through partner MassIVE as complete (Data Dependent Acquisition) or partial (Data
701 Independent Acquisition) submissions. Additional files include the complete SAINTexpress outputs for each
702 dataset and a "README" file that describes the dataset composition and the experimental procedures
703 associated with each submission. The DDA and DIA datasets generated here were each submitted as
704 independent entries. The accession numbers for the DDA dataset are MSV000095953
705 (ftp://massive.ucsd.edu/v08/MSV000095953/) in MassIVE and PXD056247 in ProteomeXchange. The
706 accession number for the DIA dataset is MSV000095944 (ftp://massive.ucsd.edu/v08/MSV000095944/).
707
708 **Data Processing**
709 The DIA-NN report.tsv file was first filtered using precursor and protein FDR thresholds of 1%
710 (Lib.Q.Value ≤ 0.01 and Lib.PG.Q.Value ≤ 0.01) to ensure high-confidence identifications. Fragment-level
711 (MS2) intensity data were extracted from the "Fragment.Quant.Raw" column in the report.tsv. Intensity
712 normalization was then performed within each bait group by adjusting for total MS2 intensity. The resulting
713 normalized fragment intensity matrix was used for SAINTq analysis to identify high-confidence interactors
714 (see Data Analysis: SAINTexpress and SAINTq to Identify Confident Interactors).

715

716 **Data Analysis: SAINTexpress and SAINTq to Identify Confident Interactors**

717 Significance Analysis of INTeractome (SAINT) is a series of computational tool used to assign
718 confidence scores to protein-protein interaction based on quantitative data generated from AP-MS and
719 BioID experiments[53]. Briefly, for each prey protein identified in a pulldown sample, SAINT calculates the
720 probability of true interaction by comparing the prey abundance detected in the sample against a set of
721 negative control pulldowns.

722 In bottom-up mass spectrometry experiments, quantification is typically achieved using either spectral
723 counting or intensity-based methods. Peptides (in DDA and DIA experiments) and fragments (uniquely in
724 DIA) are directly measured by the instruments, and protein abundance is inferred by integrating the
725 quantitative data of the corresponding peptides or fragments. The established BioID workflow employs
726 SAINTexpress to analyze protein-level spectral count data from DDA results[54]. Recent versions of SAINT
727 have been extended to analyze intensity-based data[54,67,110], with SAINTq implemented specifically for the
728 analysis of intensity data at the protein, peptide and fragment levels[67]. Although SAINTq has been available
729 since 2015, its application in BioID projects has not been widely tested. Given the richer quantitative
730 information of intensity-based data, we developed a BioID-SAINTq analysis pipeline for protein- and
731 fragment-level intensity data and benchmarked it against the established BioID-SAINTexpress.

732 *SAINTexpress Workflow:*

733 Spectral-count based analysis of DDA BioID data was performing using SAINTexpress as
734 implemented within the Fragpipe framework. The "reprint.spc.tsv" was the input for SAINTexpress and the
735 analysis was performed using the default parameters. Identified prey proteins with BFDR $\leq$ 0.05 are
736 considered high-confidence interactors.

737 *SAINTq Workflow:*

738 For DDA protein-level intensity-based analysis, the "combined_protein.tsv" file generated by Fragpipe
739 was used. After selecting the MaxLFQ intensity columns, the data were normalized by total intensity within
740 each bait group before running SAINTq (v0.0.4) with no control compression. For DIA fragment-level
741 intensity-based analysis, the total intensity normalized fragment matrix (see Data Processing) was analyzed
742 by SAINTq, with no control compression and default parameters.

743 Initial testing of SAINTq showed fewer confident interactors in DIA data despite a ~3-4 fold increased in
744 protein identifications compared to DDA. We examined the source code of SAINTq and found that when
745 calculating the difference in mean intensity (mu_d) between control samples and test samples for each
746 protein, a minimum threshold of log2(4) (2-fold change) was enforced. Any real difference less than 2 would
747 be raised to 2. While this approach might reduce noisy signals, it could over-penalize subtle interactions,
748 resulting in inflated false positive rate in FDR calculation. Given the improved quantitative power of intensity-
749 based data, we hypothesized that using the real difference for *mu_d* may lead to more accurate
750 identification of confident interactors. We modified that source code, changing
751 `std::max(test_means[i]-ctrl_means[i], std::log2(4))` to `std::max(test_means[i]-`
752 `ctrl_means[i], std::log2(1))` in main.hpp (lines 1112 and 1337). This modification resulted in
753 increased identification of confident interactors that align closely with the DDA spectral count SAINTexpress
754 workflow and published literature. Using the benchmark of known stress granule proteome and results from
755 DDA SAINTexpress, we have manually assigned BFDR 0.03 as a suitable threshold for high-confidence
756 interaction.

757 **Data Analysis: Unsupervised Hierarchical Clustering and Data Visualization**

758 To ensure the quality of DIA proteomics data prior to unsupervised hierarchical clustering, we applied a
759 two-step filtering process to each bait group. First, fragments missing in more than 80% of samples within
760 a group were excluded from the analysis. Second, precursors with fewer than three fragments were filtered
761 out. These filters were applied because fragments or precursors not quantified in the majority of samples
762 are likely noises. Next, protein intensity values were rolled up by summing intensities of corresponding
763 fragments and the resulting intensity values were log2-transformed.

764 It is important to note that stress granule baits can localize to multiple cellular compartments in the event
765 of stress. Nevertheless, if the same high-confidence interactors are consistently identified across multiple
766 baits, it can be inferred that these these interactors are likely associated with stress granules. To infer stress
767 granule -specific interactors, we filtered for 1,801 high-confidence interactors (≤ 0.03, SAINTq) that are
768 identified by at least two baits, regardless of the condition. Clusterings of bait-conditions (columns) and
769 proteins (rows) were performed using Euclidean distance and Ward's method for linkage. The R package
770 pheatmap was utilized for heatmap visualization. Finally, gene ontology (GO) enrichment analyses were

771 performed for proteins in the 4-row clusters using g:Profiler. The background protein set for the GO
772 enrichment analysis consisted of 9,860 protein entries in the spectral library as these represent the proteins
773 detectable in the experiments. GO terms with adjusted p-values ≤ 0.01 (Benjamini-Hochberg) are
774 significant.
775
776 **Data analysis: Mixed-Model Analysis of Variance**
777 The total intensity normalized fragment matrix contained a sizable proportion of missing values. To
778 improve statistical power, the matrix was imputed using a K-Nearest Neighbor (KNN) approach using the
779 python package scipy, with the number of neighbors (k) set to 5. We then used the filtered proteins from
780 two-step filtering process (see Data Analysis: Unsupervised Hierarchical Clustering and Data Visualization),
781 to select for high-quality fragments. Next, precursor intensity values were rolled up by summing intensities
782 of corresponding fragments and the resulting intensity values were log2-transformed.
783 To analyze the dynamic association of prey protein for each bait across different time points (**T1 vs**
784 **T2_AS vs T3_AS** and **T1 vs T2_NaCl vs T3_NaCl**), the following linear mixed model was applied to the
785 KNN-imputed precursor intensity matrix:
786 $$Intensity_{ij} = \beta_0 + \beta_1 \cdot Timepoint_i + u_j + \epsilon_{ij}$$
787 where $Intensity_{ij}$ represent log2-transformed intensity for precursor j at time point i. β_0 is the overall
788 intercept, β_1 is the fixed effect coefficient representing the effect of time point i, u_j is the random effect
789 accounting for variability among different precursors, and ϵ_{ij} is the residual error term. This model accounts
790 for the random effect of the precursors corresponding to the same protein and the fixed effect of the
791 timepoint. In cases where only a single precursor is available, a simpler linear model is applied without the
792 random effect:
793 $$Intensity_i = \beta_0 + \beta_1 \cdot Timepoint_i + \epsilon_i$$
794 Analysis of variance (ANOVA) was then applied to obtain p-values indicating the significance of time point
795 effects. Post-hoc analysis was conducted using estimated marginal means (EMMs) to evaluate pairwise
796 fold change between time points (i.e T1 vs T2_AS). The Benjamini-Hochberg procedure was applied to
797 correct for multiple comparisons, with differential interactions defined by p-adjusted values ≤ 0.01 and fold
798 change ≥ 1.5.

799

800 **High Content Genetic Screen of Lipoamide**

801 To generate a cell line stably expressing Cas9 and GFP-tagged FUS, A plasmid of human codon-
802 optimized *S. pyogenes* Cas9 (lentiCas9-Blast; #52962, Addgene) was transfected into HeLa Kyoto cells
803 stably expressing GFP-tagged FUS (FUS::GFP[111]), and the clone was selected with 20 μg/ml of blasticidin.
804 The cells were seeded at 550 cells/well in 384-well plates (#781092, Greiner), transfected with 20 nM
805 each of tracrRNA (U-002005, Horizon) and sgRNA from Human Edit-R crRNA library (18,710 genes tested;
806 Dharmacon) using Interferin (polyplus), and incubated for two days before the medium was replaced with
807 fresh one for 1 day. CRISPR-Cas9-mediated gene knock-out was validated with KIF11 sgRNA, which kills
808 cells. An sgRNA targeting SRSF1 (CM-018672-01, Horizon) was used to validate the assay. Mock
809 transfection was used for controls both positive and negative for stress granule formation. Three days after
810 transfection, the cells were pre-treated with 20 μM of lipoamide for 1 h and then stressed with 1 mM of
811 potassium arsenate (A6631, Sigma Aldrich) for additional 1 h in the presence of lipoamide before fixed with
812 4% formaldehyde in PBS. For only mock transfection, wells without lipoamide treatment were also prepared
813 for the positive control. The fixed cells were stained with 1 μg/ml of DAPI and 0.25 μg/ml of CellMask blue
814 (H32720, Thermo Fisher Scientific) and imaged on a CellVoyager CV7000 automated spinning disc
815 confocal microscope (Yokogawa) with a 40× NA 1.3 water objective lens.
816 For the secondary screen, the HeLa Kyoto FUS-GFP cells were seeded at 1000 cells/well in 96-well
817 plates (#655090, Greiner), transfected with 25 ng of each endoribonuclease-prepared small interfering RNA
818 (esiRNA; Eupheria) using Lipofectamine2000 (Invitrogen). Three days after transfection, the cells were
819 treated with 10 μM of lipoamide for 1 h and then stressed with 1 mM of arsenate in the presence of
820 lipoamide for 1 h before fixed with 4% formaldehyde in PBS. The cells were stained with 1 μg/ml of DAPI
821 and imaged similarly to the primary screen.

822

823 **Confocal Image Analysis**

824 For high content imaging analysis (relevant to Figures 3 and 4), segmentation of stress granules were
825 performed based on cytoplasmic FUS-GFP signals using CellProfiler[112], and the obtained information (*e.g.*,
826 number and size of stress granules, intensity of FUS::GFP) was processed with KNIME. For primary

827 genome-wide CRISPR screen, the number of stress granules per cell treated with each sgRNA was
828 normalized relative to two datasets: that of mock transfection without lipoamide treatment (defined as 100%)
829 and that of mock transfection with lipoamide treatment (0%) within each plate; the normalized values were
830 transformed into z-scores as shown in Figure 3.
831

832 **DATA AVAILABILITY**

833 All proteomics data are available at the Mass Spectrometry Interactive Virtual Environment (MassIVE,
834 http://massive.ucsd.edu). MassIVE ID: MSV00009595 (ftp://massive.ucsd.edu/v08/MSV000095953/)
835 MassIVE ID: MSV000095944 (ftp://massive.ucsd.edu/v08/MSV000095944/).
836

837 **CODE AVAILABILITY**

838 Data analysis and visualization codes will be shared upon request to the lead contact, Ji-Young Youn
839 (jiyoung.youn@sickkids.ca).
840

841 **REFERENCES**

842 1 Cheng, Z. *et al.* Differential dynamics of the mammalian mRNA and protein expression response
843 to misfolding stress. *Mol. Syst. Biol.* **12**, 855, doi:10.15252/msb.20156423 (2016).
844 2 Gomez-Pastor, R., Burchfiel, E. T. & Thiele, D. J. Regulation of heat shock transcription factors
845 and their roles in physiology and disease. *Nat. Rev. Mol. Cell Biol.* **19**, 4-19,
846 doi:10.1038/nrm.2017.73 (2018).
847 3 Christopher, J. A. *et al.* Subcellular proteomics. *Nat Rev Methods Primers* **1**, doi:10.1038/s43586-
848 021-00029-y (2021).
849 4 Lundberg, E. & Borner, G. H. H. Spatial proteomics: a powerful discovery tool for cell biology. *Nat.*
850 *Rev. Mol. Cell Biol.* **20**, 285-302, doi:10.1038/s41580-018-0094-y (2019).
851 5 Villanueva, E. *et al.* System-wide analysis of RNA and protein subcellular localization dynamics.
852 *Nat Methods* **21**, 60-71, doi:10.1038/s41592-023-02101-9 (2024).
853 6 Chong, Y. T. *et al.* Yeast Proteome Dynamics from Single Cell Imaging and Automated Analysis.
854 *Cell* **161**, 1413-1424, doi:10.1016/j.cell.2015.04.051 (2015).
855 7 Christoforou, A. *et al.* A draft map of the mouse pluripotent stem cell spatial proteome. *Nat Commun*
856 **7**, 8992, doi:10.1038/ncomms9992 (2016).
857 8 Dionne, U. & Gingras, A. C. Proximity-Dependent Biotinylation Approaches to Explore the Dynamic
858 Compartmentalized Proteome. *Front Mol Biosci* **9**, 852911, doi:10.3389/fmolb.2022.852911
859 (2022).
860 9 Go, C. D. *et al.* A Proximity-Dependent Biotinylation Map of a Human Cell. *Nature* **595**, 120-124,
861 doi:10.1038/s41586-021-03592-2 (2021).
862 10 Huh, W. K. *et al.* Global analysis of protein localization in budding yeast. *Nature* **425**, 686-691,
863 doi:10.1038/nature02026 (2003).
864 11 Itzhak, D. N., Tyanova, S., Cox, J. & Borner, G. H. Global, quantitative and dynamic mapping of
865 protein subcellular localization. *Elife* **5**, doi:10.7554/eLife.16950 (2016).
866 12 Thul, P. J. *et al.* A subcellular map of the human proteome. *Science* **356**,
867 doi:10.1126/science.aal3321 (2017).

13 Breker, M., Gymrek, M. & Schuldiner, M. A novel single-cell screening platform reveals proteome plasticity during yeast stress responses. *J. Cell Biol.* **200**, 839-850, doi:10.1083/jcb.201301120 (2013).
14 Jean Beltran, P. M., Mathias, R. A. & Cristea, I. M. A Portrait of the Human Organelle Proteome In Space and Time during Cytomegalovirus Infection. *Cell Syst* **3**, 361-373 e366, doi:10.1016/j.cels.2016.08.012 (2016).
15 Lu, A. X. *et al.* Integrating images from multiple microscopy screens reveals diverse patterns of change in the subcellular localization of proteins. *Elife* **7**, doi:10.7554/eLife.31872 (2018).
16 Tkach, J. M. *et al.* Dissecting DNA damage response pathways by analysing protein localization and abundance changes during DNA replication stress. *Nat. Cell Biol.* **14**, 966-976, doi:10.1038/ncb2549 (2012).
17 Alberti, S. & Hyman, A. A. Biomolecular condensates at the nexus of cellular stress, protein aggregation disease and ageing. *Nat. Rev. Mol. Cell Biol.* **22**, 196-213, doi:10.1038/s41580-020-00326-6 (2021).
18 Rabouille, C. & Alberti, S. Cell adaptation upon stress: the emerging role of membrane-less compartments. *Curr. Opin. Cell Biol.* **47**, 34-42, doi:10.1016/j.ceb.2017.02.006 (2017).
19 Banani, S. F., Lee, H. O., Hyman, A. A. & Rosen, M. K. Biomolecular Condensates: Organizers of Cellular Biochemistry. *Nat. Rev. Mol. Cell Biol.* **18**, 285-298, doi:10.1038/nrm.2017.7 (2017).
20 Shin, Y. & Brangwynne, C. P. Liquid phase condensation in cell physiology and disease. *Science* **357**, doi:10.1126/science.aaf4382 (2017).
21 Case, L. B., Zhang, X., Ditlev, J. A. & Rosen, M. K. Stoichiometry controls activity of phase-separated clusters of actin signaling proteins. *Science* **363**, 1093-1097, doi:10.1126/science.aau6313 (2019).
22 Franzmann, T. M. *et al.* Phase separation of a yeast prion protein promotes cellular fitness. *Science* **359**, doi:10.1126/science.aao5654 (2018).
23 Klosin, A. *et al.* Phase separation provides a mechanism to reduce noise in cells. *Science* **367**, 464-468, doi:10.1126/science.aav6691 (2020).
24 Riback, J. A. *et al.* Stress-Triggered Phase Separation Is an Adaptive, Evolutionarily Tuned Response. *Cell* **168**, 1028-1040 e1019, doi:10.1016/j.cell.2017.02.027 (2017).
25 Shin, Y. *et al.* Liquid Nuclear Condensates Mechanically Sense and Restructure the Genome. *Cell* **175**, 1481-1491 e1413, doi:10.1016/j.cell.2018.10.057 (2018).
26 Costa-Mattioli, M. & Walter, P. The integrated stress response: From mechanism to disease. *Science* **368**, doi:10.1126/science.aat5314 (2020).
27 McCormick, C. & Khaperskyy, D. A. Translation Inhibition and Stress Granules in the Antiviral Immune Response. *Nat. Rev. Immunol.* **17**, 647-660, doi:10.1038/nri.2017.63 (2017).
28 Hofmann, S., Kedersha, N., Anderson, P. & Ivanov, P. Molecular Mechanisms of Stress Granule Assembly and Disassembly. *Biochim Biophys Acta Mol Cell Res* **1868**, 118876, doi:10.1016/j.bbamcr.2020.118876 (2021).
29 Ivanov, P., Kedersha, N. & Anderson, P. Stress Granules and Processing Bodies in Translational Control. *Cold Spring Harb Perspect Biol* **11**, doi:10.1101/cshperspect.a032813 (2019).
30 Khong, A. *et al.* The Stress Granule Transcriptome Reveals Principles of mRNA Accumulation in Stress Granules. *Mol. Cell* **68**, 808-820, doi:10.1016/j.molcel.2017.10.015 (2017).
31 Millar, S. R. *et al.* A New Phase of Networking: The Molecular Composition and Regulatory Dynamics of Mammalian Stress Granules. *Chem. Rev.* **123**, 9036-9064, doi:10.1021/acs.chemrev.2c00608 (2023).
32 Kedersha, N., Ivanov, P. & Anderson, P. Stress granules and cell signaling: more than just a passing phase? *Trends Biochem. Sci.* **38**, 494-506, doi:10.1016/j.tibs.2013.07.004 (2013).
33 Panas, M. D., Ivanov, P. & Anderson, P. Mechanistic insights into mammalian stress granule dynamics. *J. Cell Biol.* **215**, 313-323, doi:10.1083/jcb.201609081 (2016).
34 Arimoto, K., Fukuda, H., Imajoh-Ohmi, S., Saito, H. & Takekawa, M. Formation of Stress Granules Inhibits Apoptosis by Suppressing Stress-Responsive MAPK Pathways. *Nat. Cell Biol.* **10**, 1324-1332, doi:10.1038/ncb1791 (2008).
35 Samir, P. *et al.* DDX3X Acts as a Live-or-Die Checkpoint in Stressed Cells by Regulating NLRP3 Inflammasome. *Nature* **573**, 590-594, doi:10.1038/s41586-019-1551-2 (2019).
36 Thedieck, K. *et al.* Inhibition of mTORC1 by astrin and stress granules prevents apoptosis in cancer cells. *Cell* **154**, 859-874, doi:10.1016/j.cell.2013.07.031 (2013).

37 Gowrishankar, G. *et al.* Inhibition of mRNA deadenylation and degradation by different types of cell stress. *Biol. Chem.* **387**, 323-327, doi:10.1515/BC.2006.043 (2006).
38 Hilgers, V., Teixeira, D. & Parker, R. Translation-independent inhibition of mRNA deadenylation during stress in Saccharomyces cerevisiae. *RNA* **12**, 1835-1845, doi:10.1261/rna.241006 (2006).
39 Horvathova, I. *et al.* The Dynamics of mRNA Turnover Revealed by Single-Molecule Imaging in Single Cells. *Mol. Cell* **68**, 615-625 e619, doi:10.1016/j.molcel.2017.09.030 (2017).
40 Kharel, P. *et al.* Stress promotes RNA G-quadruplex folding in human cells. *Nat Commun* **14**, 205, doi:10.1038/s41467-023-35811-x (2023).
41 Aulas, A. *et al.* G3BP1 Promotes Stress-Induced RNA Granule Interactions to Preserve Polyadenylated mRNA. *J. Cell Biol.* **209**, 73-84, doi:10.1083/jcb.201408092 (2015).
42 Bhattacharyya, S. N., Habermacher, R., Martine, U., Closs, E. I. & Filipowicz, W. Relief of microRNA-mediated translational repression in human cells subjected to stress. *Cell* **125**, 1111-1124, doi:10.1016/j.cell.2006.04.031 (2006).
43 Passmore, L. A. & Coller, J. Roles of mRNA poly(A) tails in regulation of eukaryotic gene expression. *Nat. Rev. Mol. Cell Biol.* **23**, 93-106, doi:10.1038/s41580-021-00417-y (2022).
44 Tudek, A. *et al.* Global view on the metabolism of RNA poly(A) tails in yeast Saccharomyces cerevisiae. *Nat Commun* **12**, 4951, doi:10.1038/s41467-021-25251-w (2021).
45 Woo, Y. M. *et al.* TED-Seq Identifies the Dynamics of Poly(A) Length during ER Stress. *Cell Rep.* **24**, 3630-3641 e3637, doi:10.1016/j.celrep.2018.08.084 (2018).
46 Yamagishi, R., Hosoda, N. & Hoshino, S. Arsenite inhibits mRNA deadenylation through proteolytic degradation of Tob and Pan3. *Biochem. Biophys. Res. Commun.* **455**, 323-331, doi:10.1016/j.bbrc.2014.11.015 (2014).
47 Dar, S. A. *et al.* Full-length direct RNA sequencing uncovers stress granule-dependent RNA decay upon cellular stress. *Elife* **13**, doi:10.7554/eLife.96284 (2024).
48 Yi, H. *et al.* PABP Cooperates with the CCR4-NOT Complex to Promote mRNA Deadenylation and Block Precocious Decay. *Mol. Cell* **70**, 1081-1088 e1085, doi:10.1016/j.molcel.2018.05.009 (2018).
49 Yamagishi, R. *et al.* Concerted action of ataxin-2 and PABPC1-bound mRNA poly(A) tail in the formation of stress granules. *Nucleic Acids Res.* **52**, 9193-9209, doi:10.1093/nar/gkae497 (2024).
50 Marmor-Kollet, H. *et al.* Spatiotemporal Proteomic Analysis of Stress Granule Disassembly Using APEX Reveals Regulation by SUMOylation and Links to ALS Pathogenesis. *Mol. Cell* **80**, 876-891, doi:10.1016/j.molcel.2020.10.032 (2020).
51 Youn, J. Y. *et al.* High-Density Proximity Mapping Reveals the Subcellular Organization of mRNA-Associated Granules and Bodies. *Mol. Cell* **69**, 517-532, doi:10.1016/j.molcel.2017.12.020 (2018).
52 Branon, T. C. *et al.* Efficient Proximity Labeling in Living Cells and Organisms with TurboID. *Nat. Biotechnol.* **36**, 880-887, doi:10.1038/nbt.4201 (2018).
53 Choi, H. *et al.* SAINT: probabilistic scoring of affinity purification-mass spectrometry data. *Nat Methods* **8**, 70-73, doi:10.1038/nmeth.1541 (2011).
54 Teo, G. *et al.* SAINTexpress: improvements and additional features in Significance Analysis of INTeractome software. *J. Proteomics* **100**, 37-43, doi:10.1016/j.jprot.2013.10.023 (2014).
55 Markmiller, S. *et al.* Context-Dependent and Disease-Specific Diversity in Protein Interactions within Stress Granules. *Cell* **172**, 590-604, doi:10.1016/j.cell.2017.12.032 (2018).
56 Uechi, H. *et al.* Small molecule modulation of a redox-sensitive stress granule protein dissolves stress granules with beneficial outcomes for familial amyotrophic lateral sclerosis models. *bioRxiv*, 721001, doi:10.1101/721001 (2024).
57 Aulas, A. *et al.* Stress-Specific Differences in Assembly and Composition of Stress Granules and Related Foci. *J. Cell Sci.* **130**, 927-937, doi:10.1242/jcs.199240 (2017).
58 Kedersha, N. *et al.* G3BP-Caprin1-USP10 complexes mediate stress granule condensation and associate with 40S subunits. *J. Cell Biol.* **212**, 845-860, doi:10.1083/jcb.201508028 (2016).
59 Bounedjah, O. *et al.* Macromolecular crowding regulates assembly of mRNA stress granules after osmotic stress: new role for compatible osmolytes. *J. Biol. Chem.* **287**, 2446-2458, doi:10.1074/jbc.M111.292748 (2012).
60 Romero-Perez, P. S., Dorone, Y., Flores, E., Sukenik, S. & Boeynaems, S. When Phased without Water: Biophysics of Cellular Desiccation, from Biomolecules to Condensates. *Chem. Rev.* **123**, 9010-9035, doi:10.1021/acs.chemrev.2c00659 (2023).
61 Shu, T. *et al.* Mesoscale molecular assembly is favored by the active, crowded cytoplasm. *bioRxiv*, doi:10.1101/2023.09.19.558334 (2023).

62 Guillen-Boixet, J. *et al.* RNA-Induced Conformational Switching and Clustering of G3BP Drive Stress Granule Assembly by Condensation. *Cell* **181**, 346-361, doi:10.1016/j.cell.2020.03.049 (2020).
63 Ivanov, P. A., Chudinova, E. M. & Nadezhdina, E. S. Disruption of microtubules inhibits cytoplasmic ribonucleoprotein stress granule formation. *Exp. Cell Res.* **290**, 227-233, doi:10.1016/s0014-4827(03)00290-8 (2003).
64 Loschi, M., Leishman, C. C., Berardone, N. & Boccaccio, G. L. Dynein and kinesin regulate stress-granule and P-body dynamics. *J. Cell Sci.* **122**, 3973-3982, doi:10.1242/jcs.051383 (2009).
65 Ludwig, C. *et al.* Data-independent acquisition-based SWATH-MS for quantitative proteomics: a tutorial. *Mol. Syst. Biol.* **14**, e8126, doi:10.15252/msb.20178126 (2018).
66 Demichev, V., Messner, C. B., Vernardis, S. I., Lilley, K. S. & Ralser, M. DIA-NN: neural networks and interference correction enable deep proteome coverage in high throughput. *Nat Methods* **17**, 41-44, doi:10.1038/s41592-019-0638-x (2020).
67 Teo, G. *et al.* SAINTq: Scoring protein-protein interactions in affinity purification - mass spectrometry experiments with fragment or peptide intensity data. *Proteomics* **16**, 2238-2245, doi:10.1002/pmic.201500499 (2016).
68 Lu, H. *et al.* Chemotherapy triggers HIF-1-dependent glutathione synthesis and copper chelation that induces the breast cancer stem cell phenotype. *Proc. Natl. Acad. Sci. U. S. A.* **112**, E4600-4609, doi:10.1073/pnas.1513433112 (2015).
69 Turakhiya, A. *et al.* ZFAND1 Recruits p97 and the 26S Proteasome to Promote the Clearance of Arsenite-Induced Stress Granules. *Mol Cell* **70**, 906-919 e907, doi:10.1016/j.molcel.2018.04.021 (2018).
70 Braun, J. E., Huntzinger, E., Fauser, M. & Izaurralde, E. GW182 proteins directly recruit cytoplasmic deadenylase complexes to miRNA targets. *Mol. Cell* **44**, 120-133, doi:10.1016/j.molcel.2011.09.007 (2011).
71 Collart, M. A. & Timmers, H. T. The eukaryotic Ccr4-not complex: a regulatory platform integrating mRNA metabolism with cellular signaling pathways? *Prog. Nucleic Acid Res. Mol. Biol.* **77**, 289-322, doi:10.1016/S0079-6603(04)77008-7 (2004).
72 Fabian, M. R. *et al.* miRNA-mediated deadenylation is orchestrated by GW182 through two conserved motifs that interact with CCR4-NOT. *Nat. Struct. Mol. Biol.* **18**, 1211-1217, doi:10.1038/nsmb.2149 (2011).
73 Flavell, A. Introns continue to amaze. *Nature* **316**, 574-575, doi:10.1038/316574a0 (1985).
74 Huntzinger, E. *et al.* The interactions of GW182 proteins with PABP and deadenylases are required for both translational repression and degradation of miRNA targets. *Nucleic Acids Res.* **41**, 978-994, doi:10.1093/nar/gks1078 (2013).
75 Ito, K. *et al.* CNOT2 depletion disrupts and inhibits the CCR4-NOT deadenylase complex and induces apoptotic cell death. *Genes Cells* **16**, 368-379, doi:10.1111/j.1365-2443.2011.01492.x (2011).
76 Raisch, T. *et al.* Distinct modes of recruitment of the CCR4-NOT complex by Drosophila and vertebrate Nanos. *EMBO J.* **35**, 974-990, doi:10.15252/embj.201593634 (2016).
77 Russell, P., Benson, J. D. & Denis, C. L. Characterization of mutations in NOT2 indicates that it plays an important role in maintaining the integrity of the CCR4-NOT complex. *J. Mol. Biol.* **322**, 27-39, doi:10.1016/s0022-2836(02)00707-6 (2002).
78 Boeynaems, S. *et al.* Spontaneous driving forces give rise to protein-RNA condensates with coexisting phases and complex material properties. *Proc. Natl. Acad. Sci. U. S. A.* **116**, 7889-7898, doi:10.1073/pnas.1821038116 (2019).
79 Eisenberg, H. & Felsenfeld, G. Studies of the temperature-dependent conformation and phase separation of polyriboadenylic acid solutions at neutral pH. *J. Mol. Biol.* **30**, 17-37, doi:10.1016/0022-2836(67)90240-9 (1967).
80 Jain, A. & Vale, R. D. RNA phase transitions in repeat expansion disorders. *Nature* **546**, 243-247, doi:10.1038/nature22386 (2017).
81 Van Treeck, B. *et al.* RNA Self-Assembly Contributes to Stress Granule Formation and Defining the Stress Granule Transcriptome. *Proc. Natl. Acad. Sci. U. S. A.* **115**, 2734-2739, doi:10.1073/pnas.1800038115 (2018).
82 Wadsworth, G. M. *et al.* RNAs undergo phase transitions with lower critical solution temperatures. *Nat. Chem.* **15**, 1693-1704, doi:10.1038/s41557-023-01353-4 (2023).

83 Kondrashov, A. *et al.* Inhibition of polyadenylation reduces inflammatory gene induction. *RNA* **18**, 2236-2250, doi:10.1261/rna.032391.112 (2012).
84 Burgess, H. M. *et al.* CCR4-NOT differentially controls host versus virus poly(a)-tail length and regulates HCMV infection. *EMBO Rep* **24**, e56327, doi:10.15252/embr.202256327 (2023).
85 Suzuki, T. *et al.* Regulation of CCR4-NOT complex deadenylase activity and cellular responses by MK2-dependent phosphorylation of CNOT2. *RNA Biol.* **19**, 234-246, doi:10.1080/15476286.2021.2021676 (2022).
86 Cougot, N., Babajko, S. & Seraphin, B. Cytoplasmic foci are sites of mRNA decay in human cells. *J. Cell Biol.* **165**, 31-40, doi:10.1083/jcb.200309008 (2004).
87 Zheng, D. *et al.* Deadenylation is prerequisite for P-body formation and mRNA decay in mammalian cells. *J. Cell Biol.* **182**, 89-101, doi:10.1083/jcb.200801196 (2008).
88 Kedersha, N. *et al.* Stress granules and processing bodies are dynamically linked sites of mRNP remodeling. *J Cell Biol* **169**, 871-884, doi:10.1083/jcb.200502088 (2005).
89 Jain, S. *et al.* ATPase-Modulated Stress Granules Contain a Diverse Proteome and Substructure. *Cell* **164**, 487-498, doi:10.1016/j.cell.2015.12.038 (2016).
90 Costanzo, M. *et al.* A global genetic interaction network maps a wiring diagram of cellular function. *Science* **353**, doi:10.1126/science.aaf1420 (2016).
91 VanderSluis, B. *et al.* Integrating genetic and protein-protein interaction networks maps a functional wiring diagram of a cell. *Curr. Opin. Microbiol.* **45**, 170-179, doi:10.1016/j.mib.2018.06.004 (2018).
92 Matheny, T., Van Treeck, B., Huynh, T. N. & Parker, R. RNA Partitioning into Stress Granules is Based on the Summation of Multiple Interactions. *RNA* **27**, 174-189, doi:10.1261/rna.078204.120 (2021).
93 Bianchin, C., Mauxion, F., Sentis, S., Seraphin, B. & Corbo, L. Conservation of the deadenylase activity of proteins of the Caf1 family in human. *RNA* **11**, 487-494, doi:10.1261/rna.7135305 (2005).
94 Yamashita, A. *et al.* Concerted action of poly(A) nucleases and decapping enzyme in mammalian mRNA turnover. *Nat. Struct. Mol. Biol.* **12**, 1054-1063, doi:10.1038/nsmb1016 (2005).
95 Kim, T. H. *et al.* Phospho-dependent phase separation of FMRP and CAPRIN1 recapitulates regulation of translation and deadenylation. *Science* **365**, 825-829, doi:10.1126/science.aax4240 (2019).
96 Dar, S. A. *et al.* Full-length direct RNA sequencing uncovers stress-granule dependent RNA decay upon cellular stress. *bioRxiv*, doi:10.1101/2023.08.31.555629 (2024).
97 Franzmann, T. M. & Alberti, S. Protein Phase Separation as a Stress Survival Strategy. *Cold Spring Harb. Perspect. Biol.* **11**, doi:10.1101/cshperspect.a034058 (2019).
98 Kik, S. K. *et al.* An adaptive biomolecular condensation response is conserved across environmentally divergent species. *bioRxiv*, doi:10.1101/2023.07.28.551061 (2023).
99 Sasazawa, M., Tomares, D. T., Childers, W. S. & Saurabh, S. Biomolecular condensates as stress sensors and modulators of bacterial signaling. *PLoS Pathog.* **20**, e1012413, doi:10.1371/journal.ppat.1012413 (2024).
100 Schreiber, K. J., Kadijk, E. & Youn, J. Y. Exploring Options for Proximity-Dependent Biotinylation Experiments: Comparative Analysis of Labeling Enzymes and Affinity Purification Resins. *J Proteome Res* **23**, 1531-1543, doi:10.1021/acs.jproteome.3c00908 (2024).
101 Schmidt, E. K., Clavarino, G., Ceppi, M. & Pierre, P. SUnSET, a nonradioactive method to monitor protein synthesis. *Nat Methods* **6**, 275-277, doi:10.1038/nmeth.1314 (2009).
102 Youn, J. Y. *et al.* Properties of Stress Granule and P-Body Proteomes. *Mol. Cell* **76**, 286-294, doi:10.1016/j.molcel.2019.09.014 (2019).
103 Pino, L. K., Just, S. C., MacCoss, M. J. & Searle, B. C. Acquiring and Analyzing Data Independent Acquisition Proteomics Experiments without Spectrum Libraries. *Mol. Cell. Proteomics* **19**, 1088-1103, doi:10.1074/mcp.P119.001913 (2020).
104 Yang, K. L. *et al.* MSBooster: improving peptide identification rates using deep learning-based features. *Nat Commun* **14**, 4539, doi:10.1038/s41467-023-40129-9 (2023).
105 The, M., MacCoss, M. J., Noble, W. S. & Kall, L. Fast and Accurate Protein False Discovery Rates on Large-Scale Proteomics Data Sets with Percolator 3.0. *J. Am. Soc. Mass Spectrom.* **27**, 1719-1727, doi:10.1007/s13361-016-1460-7 (2016).
106 Nesvizhskii, A. I., Keller, A., Kolker, E. & Aebersold, R. A statistical model for identifying proteins by tandem mass spectrometry. *Anal. Chem.* **75**, 4646-4658, doi:10.1021/ac0341261 (2003).

107 Yu, F., Haynes, S. E. & Nesvizhskii, A. I. IonQuant Enables Accurate and Sensitive Label-Free Quantification With FDR-Controlled Match-Between-Runs. *Mol. Cell. Proteomics* **20**, 100077, doi:10.1016/j.mcpro.2021.100077 (2021).
108 Yu, F. *et al.* Fast Quantitative Analysis of timsTOF PASEF Data with MSFragger and IonQuant. *Mol. Cell. Proteomics* **19**, 1575-1585, doi:10.1074/mcp.TIR120.002048 (2020).
109 Schubert, O. T. *et al.* Building high-quality assay libraries for targeted analysis of SWATH MS data. *Nat. Protoc.* **10**, 426-441, doi:10.1038/nprot.2015.015 (2015).
110 Choi, H. *et al.* Analyzing protein-protein interactions from affinity purification-mass spectrometry data with SAINT. *Curr Protoc Bioinformatics* **Chapter 8**, 8 15 11-18 15 23, doi:10.1002/0471250953.bi0815s39 (2012).
111 Poser, I. *et al.* BAC TransgeneOmics: a high-throughput method for exploration of protein function in mammals. *Nat Methods* **5**, 409-415, doi:10.1038/nmeth.1199 (2008).
112 McQuin, C. *et al.* CellProfiler 3.0: Next-generation image processing for biology. *PLoS Biol.* **16**, e2005970, doi:10.1371/journal.pbio.2005970 (2018).

ACKNOWLEDGEMENT

We thank B. Larsen, C. Wong, G. Liu, V. Kasmaeifar, H.W. Choi, and A.C. Gingras for help with proteomics and SAINTq analysis; K. Talipova and Laurence Pelletier for contribution to validation. We thank John Rubinstein for his critical review of the manuscript. This work was supported by the Natural Sciences and Engineering Research Council of Canada (NSERC; RGPIN-2022-04849), Canada Foundation for Innovation (CFI; 41430) and the Canadian Institutes of Health Research (481147) to J.-Y.Y. Confocal imaging was performed at the SickKids Imaging Facility, a facility supported by Canada Foundation for Innovation, Ontario Research Fund and SickKids Research Institute. J.-Y.Y is the Canada Research Chair (Tier 2) in Membraneless Organelle Proteomics.

AUTHOR CONTRIBUTIONS

Conceptualization, J.-Y.Y., A. H.; Methodology, Y.-C.T., H.U., S.R.M., E.K., K.J.S., R.B., C.M., A.J.; Software, Y.-C.T.; Validation, E.K., A.M.; Formal Analysis, Y.-C.T., H.U., S.R.M., K.J.S.; Investigation, Y.-C.T., H.U., S.R.M., E.K., K.J.S., A.M., Z.Z., J.S.; Resources, J.Q.H.; Data Curation, Y.-C.T.; Writing – Original Draft, J.-Y.Y., H.U., Y.-C.T.; Writing – Review & Editing, H.U., Y.-C.T., E.K., A.M., K.J.S., J.Q.H., H.R., A.H., J.-Y.Y.; Visualization, Y.-C.T., H.U., J.-Y.Y.; Supervision, J.-Y.Y., H.R., A. H.; Project Administration, J.-Y.Y. H.R., H.U., A. H.; and Funding Acquisition, J.-Y.Y., H.R., A. H.

1125 **DECLARATION OF INTERESTS**

1126 A.A.H. is a founder and scientific adviser board member of Dewpoint Therapeutics.

1127

1128 **DECLARATION OF GENERATIVE AI AND AI-ASSISTED TECHNOLOGIES**

1129 ChatGPT was employed to improve writing style and grammar checks. The authors carefully reviewed,
1130 edited, and revised the content according to their own preferences, assuming ultimate responsibility for the
1131 publication's content.

1132

1133 **SUPPLEMENTAL INFORMATION**

1134 **Figure S1. Stress BioID quality control** (**a**) Western blot analysis comparing the levels of stably expressed
1135 miniTurbo-tagged proteins to the corresponding endogenous proteins. Lysates prepared from HEK293 Flp-
1136 In TREx parental cell line, tetracycline-induced miniTurbo stable cells or uninduced cells were analyzed for
1137 each stress granule bait protein (top). Ponceau staining of the total blot is used as a loading control (bottom).
1138 Left: G3BP1 and Right: FMR1. (**b**) Immunofluorescence microscopy of miniTurbo-3xFLAG-G3BP1 cells
1139 untreated or stressed with sodium arsenite, then BioID labeled. Stress granule marker (TIA1), bait (FLAG)
1140 and biotinylated proteins (Strep). Scale bar = 10 μM. (**c**) Lipoamide titration test to determine effective
1141 concentration for stress granule inhibition in BioID cells. Quantifications from 2,600-4,300 cells. (**d**)
1142 Condition-condition plot of miniT-G3BP1 high-confidence proximal interactors in cells incubated with a
1143 carrier (DMSO) or 100mM lipoamide for 1hr, then biotin labelling in steady state. (**e**) Venn diagram
1144 comparison of high-confident preys identified from 58 high-specificity baits from Youn *et al.,* 2018 (red),
1145 high-confidence preys of selected nine baits (green) and literature-curated stress granule proteome (Tier
1146 1; Youn *et al.,* 2019).

1147

1148 **Figure S2. Stress granule assembly and disassembly kinetics.** (**a**) Immunofluorescence microscopy
1149 images of HEK293 Flp-In T-REx cells fixed and stained for stress granules (G3BP1) at 1hr (left) or 1.5hr
1150 after recovery post oxidative stress. Scale bar = 10 μM. (**b**) Immunofluorescence microscopy images show
1151 stress granule condensation kinetics after hyperosmotic stress (0.2 M NaCl) for indicated times in HEK293
1152 Flp-In T-REx cells. Stress granule marker G3BP1 (green); P-body marker EDC3 (red); Nuclei (DAPI). Scale
1153 bar = 10 μM. (**c**) Western blot analysis examining the activation of integrated stress response in HEK293
1154 Flp-In T-REx cells during steady state, oxidative (500 μM sodium arsenite, SA) or hyperosmotic (0.2 M
1155 sodium chloride, NaCl). (**d**) Subcellular localization of BioID bait (FLAG), biotinylated proximal proteins
1156 (Strep), and stress granules (TIA1) after 30 min of biotin labeling in hyperosmotic stress condition in miniT-
1157 3xFLAG-G3BP1 HEK293 cells. Scale bar = 10 μM. (**e**) Stress granule dissolution kinetics after
1158 hyperosmotic stress in HEK293 Flp-In T-REx cells at 1 min (left) or 30 min after recovery. Scale bar = 10

1159 μM. (**f**) Schematics of biotin labeling performed in stress BioID timecourse experiments. (**g**) Western blot
1160 analysis of puromycin incorporation for 10 min during the indicated stress and recovery periods. UT =
1161 untreated (steady state), AS = sodium arsenite (500 μM, 35 min), NaCl (0.2M NaCl, 35 min).
1162
1163 **Figure S3. Hyperosmotic stress induces proximal associations with microtubule-associated**
1164 **proteins.**
1165 (**a**) Overview of number of stress BioID experiments performed. (**b**) Dot plot visualization of selected high-
1166 confidence preys identified in DDX3X stress BioID timecourse. AS = sodium arsenite (500μM, 5'-35'), NaCl
1167 (0.2M NaCl, 45'-75'). (**c**) Schematics show alternative hyperosmotic stress timecourse set up (top). Dot plot
1168 visualization of selected high-confidence preys identified by DDX3X during alternative hyperosmotic stress
1169 conditions (bottom). (**d**) Heatmap visualization of hierarchical clustering of high-confidence preys identified
1170 in DCP1A and DDX3X stress BioID. Baits and conditions are clustered on the x-axis, and high-confidence
1171 interactors are clustered on the y-axis based on their abundance.
1172
1173 **Figure S4. DIA analysis improves data quality.** (**a**) Illustration of Data-Dependent Acquisition (DDA) *vs.*
1174 Data-Independent Acquisition (DIA) methods in mass spectrometry. (**b**) Diagram of BioID DIA analysis
1175 workflow. (**c**) Bar graph of identified proteins in each BioID time-course experiment using DDA and DIA
1176 methods. Error bars show variation between replicates. (**d**) Boxplot shows the pairwise Jaccard indices
1177 between BioID samples. Each point represents a pairwise sample comparison. (**e**) Bar graph shows
1178 comparison to other existing datasets. Colours indicate overlap with literature-curated stress granule
1179 proteins (red), shared with another dataset but not annotated as stress granule proteins (orange), and
1180 unique to each dataset (blue). Youn *et al.,* 2018 dataset includes high-confidence interactors identified in
1181 58 stress granule steady state BioID experiments. (**f**) The violin plot shows the distributions of abundance
1182 fold-changes in high-confidence interactors during stress timecourse. (**g**) Colocalization validation of
1183 identified high-confidence interactors to stress granules in HeLa Flp-In T-REx cells. TRIM56 (endogenous);
1184 LARP6-mCherry (stable expression). Scale bar = 10 μM. (**h**) Volcano plot shows abundance changes in
1185 G3BP1 high-confidence interactors during steady to stress state transition.
1186
1187 **Figure S5. Subcellular localization of CCR4-NOT complex.** (**a**) Immunofluorescence microscopy of
1188 HEK293 Flp-In T-REx cells in unstressed or stressed conditions (500 μM sodium arsenite, 30 min or 0.2 M
1189 sodium chloride, 1 hr). CNOT1 (green), P-body marker EDC3 (red), nuclei (DAPI). Scale bar = 10 μM. (**b**)
1190 Immunofluorescence microscopy of HEK293 Flp-In T-REx cells in unstressed or stressed conditions (500
1191 μM sodium arsenite, 30 min or 0.2 M sodium chloride, 1 hr). CNOT1, CNOT7, or CNOT8 (red) paired with
1192 stress granule marker G3BP1 (green), nuclei (DAPI). Intensity line plot made in Fiji. Scale bar = 10 μM. (**c**)
1193 Immunofluorescence microscopy of CNOT2-3xFLAG stable cells untreated or stressed for 30 minutes,
1194 stained for stress granule marker (G3BP1) and FLAG tag on CNOT2-3xFLAG construct. Scale bar = 10
1195 μM.

1196

1197 **Table S1.** Stress BioID of G3BP1 and FMR1 during oxidative stress and Stress BioID of G3BP1 with
1198 lipoamide pre-treatment, related to Figure 1.
1199 **Table S2.** High Information Bait Selection, related to Figure 2A.
1200 **Table S3.** Stress BioID of Nine Stress Granule, Stress Granule/P-body baits during stress analyzed in DDA
1201 mode, related to Figure 2C and Figure S3.
1202 **Table S4.** Stress BioID of Nine Stress Granule, Stress Granule/P-body baits during stress analyzed in DIA
1203 mode, related to Figure 2E.
1204 **Table S5.** Hierarchial Clustering Analysis of Conserved High-Confidence Proximal Interactors, related to
1205 Figures 2F-G.
1206 **Table S6.** Linear Mixed Model ANOVA Analysis to Determine Differentially Interacting Proximal Interactors,
1207 related to Figure 2H.
1208 **Table S7.** Genome-wide CRISPR screen, validation and cordycepin experiments, related to Figures 3-4.
1209

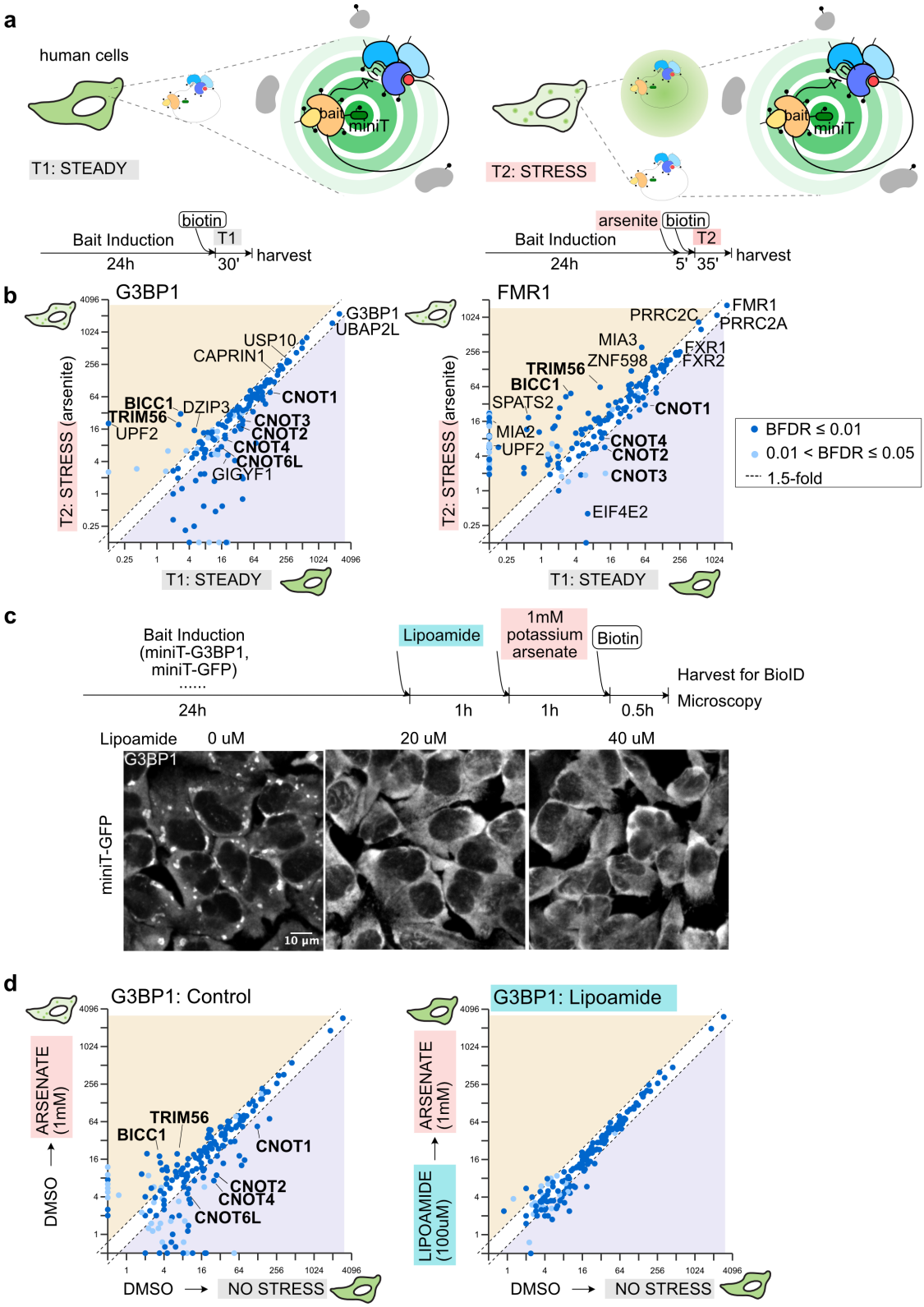

Fig 1. BioID of Stress Granules during steady state and stress (**a**) Schematics show experimental workflow of stress granule proximity labelling at steady (left) or stressed state with oxidative stress (right)

1213 in human cells. (**b**) Quantitative comparison of average spectra (log2 transformed) of high-confidence
1214 interactors identified by G3BP1 (left) and FMR1 (right) during steady vs. stress state (0.5mM sodium
1215 arsenite). (**c**) Lipoamide titration test to determine the effective concentration for proximity labeling. (**d**)
1216 Comparative analyses of carrier pre-treated stress BioID (left) *vs.* lipoamide pre-treated stress BioID (right).
1217 The condition-condition plot shows the average spectra (log2 transformed) of high-confident interactors
1218 identified by G3BP1.
1219

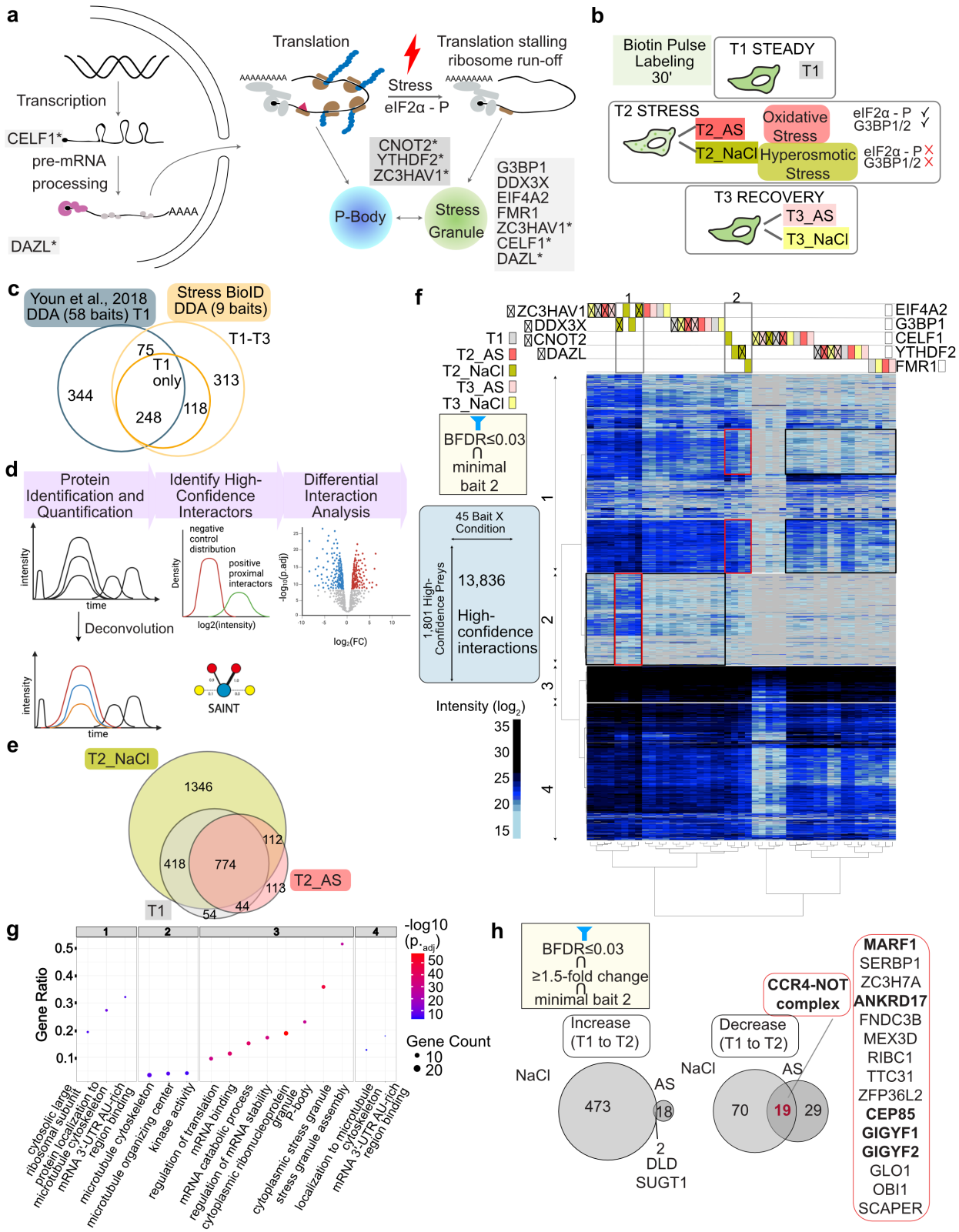

Fig 2. Dynamic proteomic landscapes of stress granules (**a**) Schematics of nine high-information baits and their subcellular location. Baits with asterisks localize to multiple compartments. (**b**) Diagram of stress

1223 BioID experimental workflow. Proximity labelling is performed during steady, stress (AS = arsenite;
1224 oxidative stress, or NaCl; hyperosmotic stress), or recovery periods for 30 min. (**c**) Venn diagram
1225 visualization of overlap between high-confidence interactors identified in published BirA* DDA data (58
1226 baits) *vs.* miniT DDA data generated in this study. (**d**) Diagram depicting stepwise DIA data analysis pipeline
1227 to improve identification and quantification. (**e**) Venn diagram summarizes the overlap between high-
1228 confidence interactors identified in steady state (T1), T2 in oxidative stress (T2_AS), and hyperosmotic
1229 stress (T2_NaCl). (**f**) Heatmap display of hierarchical clustering analysis of statistically significant proximal
1230 interactors identified by at least two baits in stress BioID DIA data (BFDR≤0.03). Baits and conditions are
1231 clustered on the x-axis, and high-confident interactors are clustered on the y-axis based on their
1232 abundance. (**g**) Dot Plot visualizes the Gene Ontology terms enriched in each cluster indicated in panel (f).
1233 (**h**) Venn diagram of high-confident interactors displaying ≥1.5-fold change in two baits or more from steady
1234 (T1) to stress condition (T2).
1235

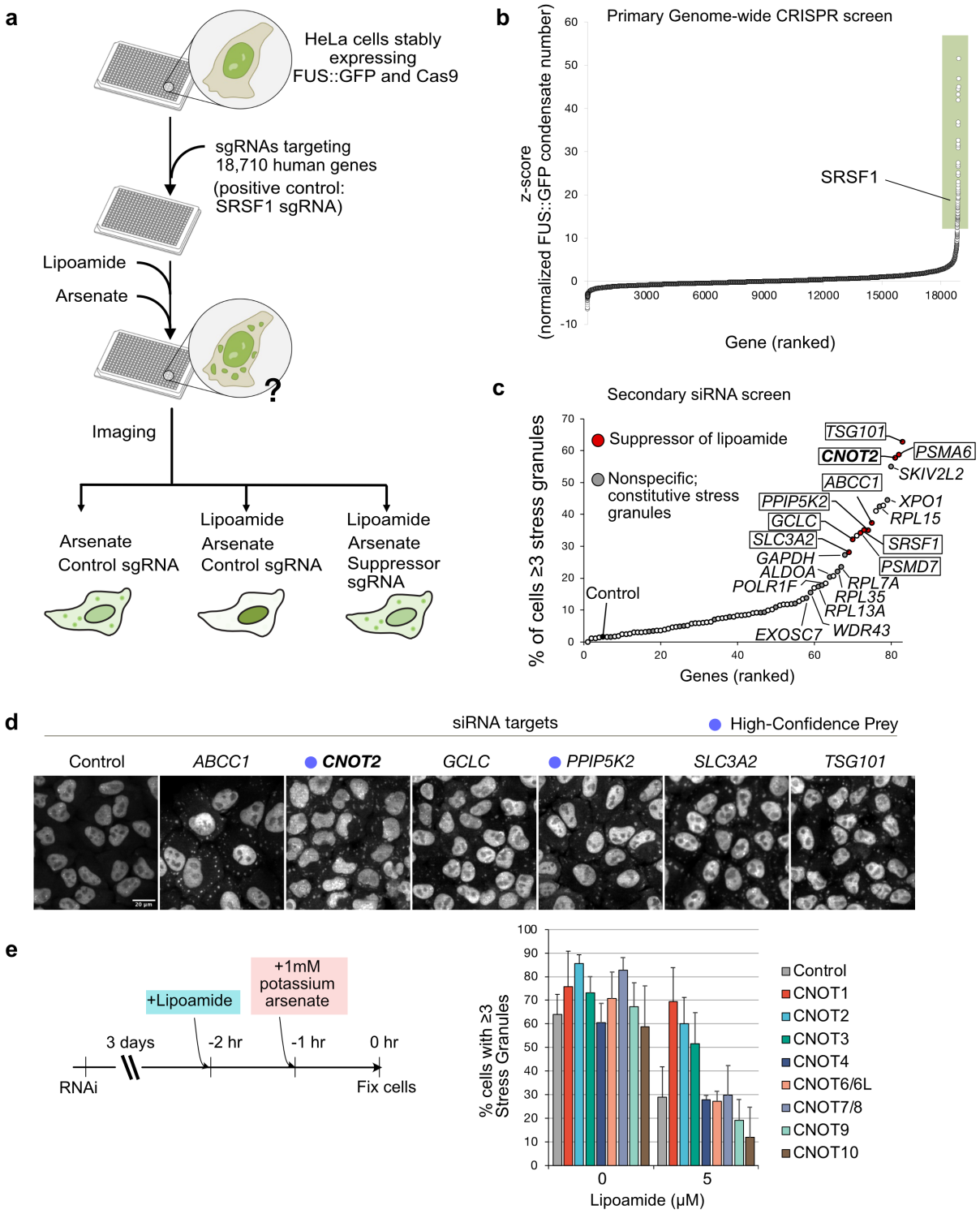

Fig 3. A genome-wide suppressor screen identifies components that bypass the effect of lipoamide on stress granules. (**a**) Schematics showing genome-wide CRISPR Cas knock-out screen to identify

1239 genes that block the inhibitory activity of lipoamide on stress granule formation. (**b**) A rank-ordered
1240 visualization of candidate genes whose knock-out results in suppression of lipoamide activity, including its
1241 known target, SRSF1. (**c**) Secondary siRNA screen results show lipoamide suppressors validated in the
1242 oxidative stress condition, outlined in boxes (filled in red). Nonspecific suppressor results in constitutive
1243 induction of stress granules in the absence of stress (filled in gray); a subset is listed. (**d**) Representative
1244 images of validated lipoamide suppressors. Scale bar = 20μM. Magenta dot: high-confidence stress granule
1245 interactors. (**e**) Examination of individual CCR4-NOT complex components on their requirements for
1246 lipoamide activity on stress granules using siRNA-mediated knockdown in HeLa cells. The average
1247 percentage of cells with three or more cytosolic FUS-GFP puncta when pretreated with siRNA and
1248 lipoamide prior to stress. Quantification from three biological replicates.
1249

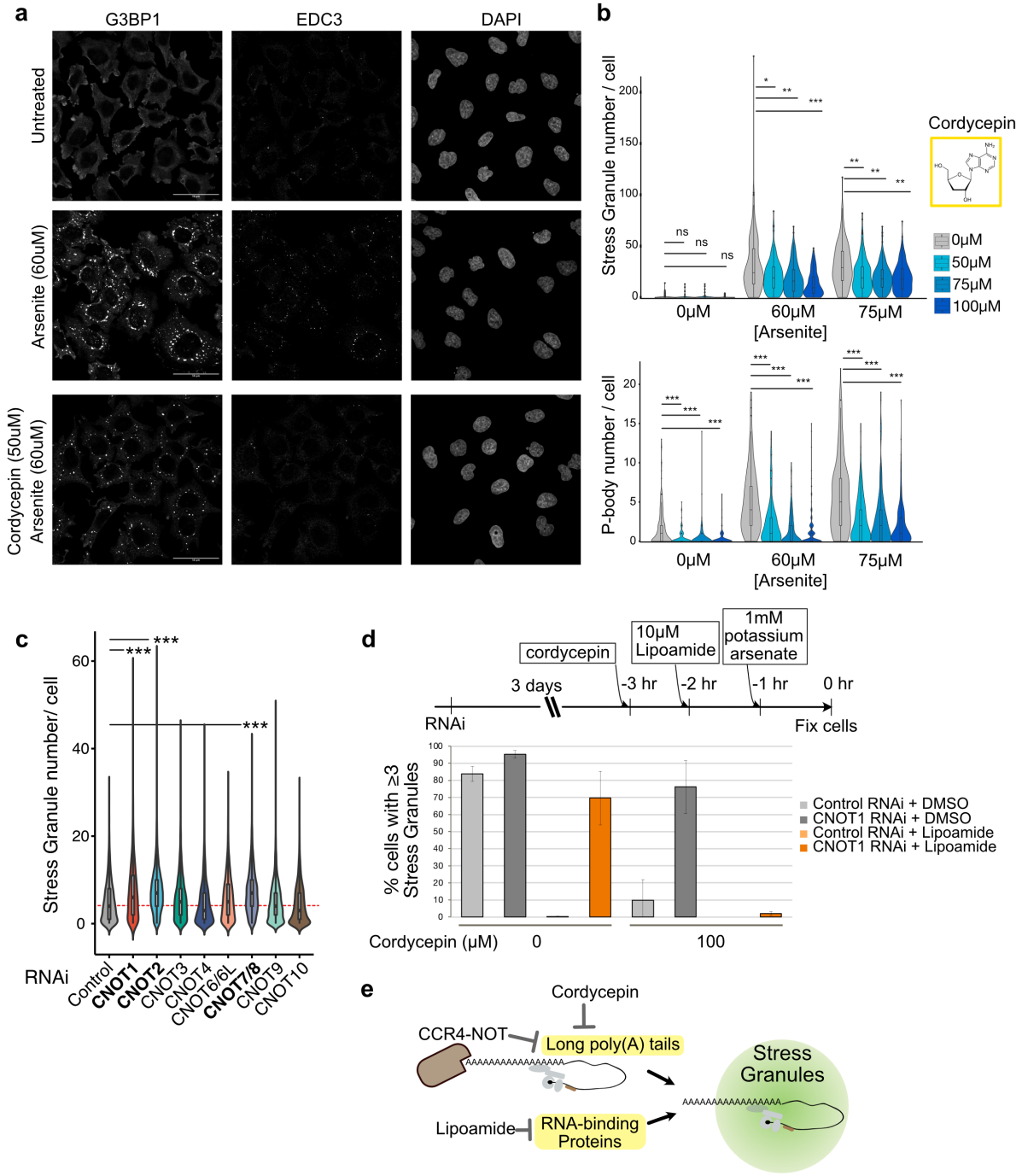

Fig 4. Altering Poly(A) lengths affects stress granule formation. (**a**) Representative images show the effect of cordycepin pretreatment on stress granules (G3BP1) and P-bodies (EDC3) in HeLa Flp-In T-REx cells (50 μM cordycepin 3 hrs with 60 μM sodium arsenite treatment during the last hour). Scale bar = 50 μM. (**b**) Violin-box plot shows stress granule and P-body numbers in cells pretreated with cordycepin before stress (cordycepin for 3 hrs with sodium arsenite stress for the final hour). Mann Whitney test on three biological replicates (* $p_{adj} < 10^{-3}$, ** $p_{adj} < 10^{-5}$, *** $p_{adj} < 10^{-10}$). (**c**) Violin-box plot shows cytoplasmic

1256 FUS::GFP granule numbers in siRNA-treated cells under oxidative stress (1mM arsenate, 1hr). Mann-
1257 Whitney test of three biological replicates (*** $p_{adj} < 10^{-10}$). The median stress granule number in control is
1258 indicated in a red dotted line. (**d**) Schematics show the sequence of treatments (top). Bar graph shows the
1259 percentage of cells containing ≥3 stress granules in HeLa cells treated with conditions prior to stress
1260 (CNOT1 RNAi, cordycepin, or lipoamide; bottom). Three biological replicates (n >300). (**e**) Model of two
1261 paralleled mechanisms driving stress granule formation. Lengthening global poly(A) tails promotes stress
1262 granule formation, which the CCR4-NOT deadenylase complex or cordycepin inhibits. Conformational
1263 changes in RNA-binding proteins promote stress granule formation, which is inhibited by lipoamide[56].
1264

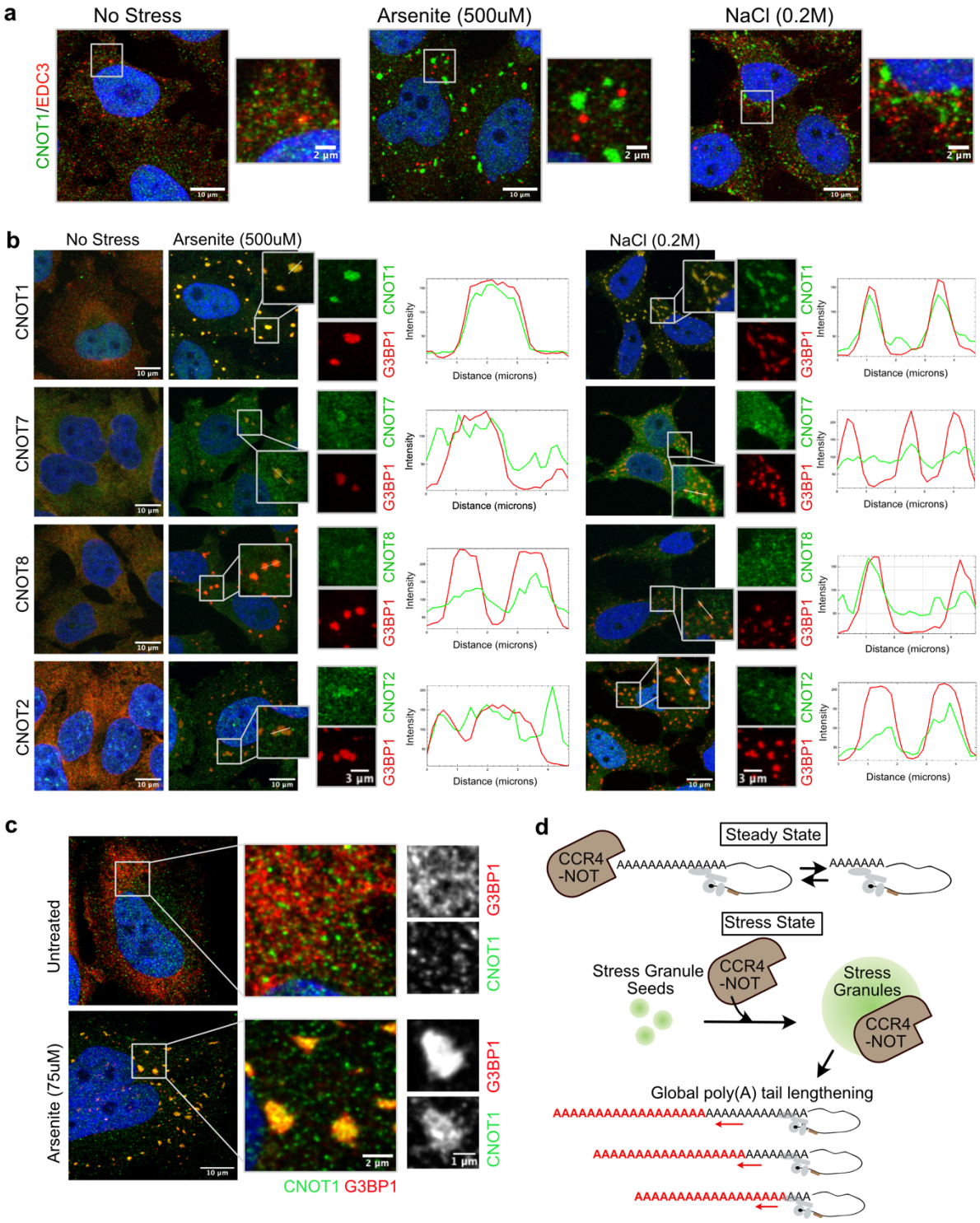

Fig 5. Stress Granule localization of the CCR4-NOT complex. (**a**) Immunofluorescence microscopy of CNOT1 (green), P-body marker EDC3 (red), and nuclei (DAPI) in HeLa cells at steady state and stress

1268 conditions (500 μM sodium arsenite, 30 min or 0.2 M sodium chloride, 1 hr). Scale bar = 10 μM. (**b**)
1269 Immunofluorescence microscopy of CNOT1, CNOT2, CNOT7 and CNOT8 (green), stress granule marker
1270 G3BP1 (red), and nuclei (DAPI) during oxidative (sodium arsenite, 500μM, 30 min) and hyperosmotic stress
1271 (sodium chloride, 0.2 M, 1hr) in HeLa cells. Line plots represent the fluorescent intensity included in the
1272 selected insets. Scale bars = 10 μM and 3 μM (from left to right zoomed insets). (**c**) Lightning mode confocal
1273 microscopy of CNOT1 (green), stress granule marker G3BP1 (red), and nuclei (DAPI) during oxidative
1274 stress (sodium arsenite, 75 μM, 1hr) and at steady state in HeLa cells. Scale bars = 10, 2 and 1μM (from
1275 left to right zoomed insets). (**d**) Schematics show a proposed global poly(A) lengthening model during
1276 stress. During steady state, the CCR4-NOT deadenylase complex is active and trims the transcriptome's
1277 poly(A) tails. Upon stress, the CCR4-NOT complex is sequestered to stress granules, resulting in the global
1278 lengthening of poly(A) tails.
1279
1280